Experimental Evaluation of a Solid-State Organ-Targeted Positron Emission Tomography (PET) Camera

Abstract

Positron Emission Tomography (PET) with an organ-targeted approach has a potential to significantly improve the diagnosis of a variety of diseases through higher detection efficacy and a reduced dose of radioactivity than when conventional whole-body (WB) PET systems are used. The application of functional imaging with organ-targeted PET to breast-cancer screening and diagnosis brings with it the benefits of visualizing malignant growths at the early stages of the disease as well as being unaffected by dense breast tissue. This acts as a workaround to one of the most notable current issues with anatomical X-ray imaging techniques for breast cancer of having a lower specificity of detection because of masking effects of dense cancerous tissues with a similarly dense tissue background.

Experimental evaluation of a novel solid-state PET detector technology, called the Radialis PET camera, has demonstrated that through the modular architecture of PET flat-panel detectors, system performance parameters including spatial resolution, sensitivity, and detector count rates can be improved significantly. In clinical settings these improvements are translated into accurate detectability of small cancerous lesions even at a 10-fold reduction in radiotracer activity in comparison with standard WB PET dose and therefore, will ultimately allow for the implementation of organ-targeted low-dose PET imaging to breast cancer screening, diagnosis, and treatment follow-up.

The provided performance evaluation is carried out through the system performance characteristics defined by the National Electrical Manufacturers Association (NEMA) NU-4 tests for small animal PET systems. Although the methods of NEMA NU-4 are defined for pre-clinical small-

animal PET systems, they are easily adopted for an organ-targeted architecture with minimal changes to the experimental methods or the analysis techniques. The spatial resolution of the Radialis PET camera is measured to be (2.3 ± 0.1) mm and is verified to result in much higher quality images than WB PET. Measured absolute per-slice sensitivity is 3.5% in the center of the field-of-view (FOV) and is the current best-in-class for any breast-targeted system currently available. This marks the most important result, which was determined based on the NEMA analysis. The high sensitivity of this device promises to mitigate one of the main drawbacks of radiation functional imaging, being the high administered radioactive dose to patients. The count rates were determined to be 17.8 kcps for the noise equivalent count rate (NECR) and 32.5 kcps for the peak true count rates, at a phantom activity concentration of 0.01 MBq/mL which corresponds to the upper range of clinically relevant activities. This further justifies the capability for an efficient gamma-detection under low doses of administered radiopharmaceuticals.

Following the standardized analysis outlined above, an investigation into the image quality of the PET camera is conducted with image quality phantoms, and an evaluation of image uniformity and the recovery coefficients which are needed to quantify the response of gamma detectors to a spatially uniform flux of incident radiation over the FOV and the detectability of small lesions respectively. Finally, selected clinical images of patients with a newly diagnosed breast cancer acquired in the framework of the pilot clinical trials are presented to demonstrate an improved lesion detectability and specificity in comparison with standard imaging technologies.

Table of Contents

5

Table of Figures

7

9

10

Table of Tables

11

Acknowledgments

I would like to thank, first and foremost, my scientific supervisor Dr. Alla Reznik for the formative opportunities that she has provided for me and for the invaluable learning experiences that I have experienced as part of this Master's Thesis. Her mentorship and approach to my learning has left me with experiences, both scientifically and professionally, which will stay with me forever and for that I am eternally grateful. The outcome of this work is certainly made successful by the steady and unfaltering effort that she provided for my project.

Dr. Sasha Bubon and Dr. Harutyun Poladyan were both instrumental in my progress with their experienced support and scientific expertise. I am grateful to both for their discussions and assistance throughout the entirety of my thesis work.

I am also thankful to my supervisory committee, Dr. Apichart Linhananta and Dr. Mitchel Albert, for agreeing to support me and for taking the time to provide their constructive feedback.

I want to thank Radialis Medical for their collaboration, and for providing the technology and the components required for my experimentation. They provided the system with which I helped to develop and test in my work.

Thank you to Lakehead University and the Physics Department for providing me this opportunity and to the Thunder Bay Regional Health Research Institute for giving me a facility for my research.

Finally, I want to thank my parents Jeff, and Sandra Stiles, for supporting me through my whole education and for helping me get through my degree. Without them I surely wouldn't have succeeded.

1 Section 1 – Principles of Positron Emission Tomography

1.1 Introduction to Positron Emission Tomography

Positron emission tomography (PET) is a molecular imaging technique which is used for the characterization of functional (biological) processes in the body. This practice uses an injection of radiolabeled biomarkers (or radiotracers) into a patient, which are designed to accumulate in specific regions of the body to identify abnormal biological behaviors. PET has several benefits over anatomical imaging for clinical application (ie: X-ray imaging) as it allows for a very accurate detection[1], as well as being a reliable tool for the monitoring of treatment efficacy[2], due to the relationship between the extent of the disease and the observed radiotracer uptake.

The radiotracer that is used for PET imaging depends on the specific clinical need, however for a majority of cases PET is used for imaging cancer and is almost exclusively performed with [^{18}F]-fluorodeoxyglucose (FDG). FDG is a glucose molecule that is labeled with a radioactive ^{18}F atom as a replacement for one hydroxyl (OH) group of the molecule. FDG is injected intravenously, and due to an increased metabolic uptake of glucose (which is characteristic of cancerous tissues), will accumulate in malignant cells and emit gamma radiation from the decay of the ^{18}F nucleus. Because of the increased radiotracer uptake in relation to benign surrounding tissues, cancerous lesions end up becoming much more radioactive than background tissues: lesions can accumulate up to 10x-15x more radioactivity than the surrounding background tissues and this excess of the radioactivity can be detected on PET images to identify areas of increased glucose metabolism.

The half-life for ^{18}F is 110 minutes and allows for prompt acquisitions of patients due to the relatively short time required for the radioactive decay to occur. The mode of decay for ^{18}F is through positron emission with a branching fraction of 97%, or through electron capture with a branching fraction of 3%. Positrons have a rest mass of 511 keV and can have a maximum kinetic energy of 635 keV after the decay from ^{18}F[3]. This excess energy causes the positron to travel away from the parent nucleus, inelastically scattering through the medium and rapidly losing its kinetic energy. The average distance from the parent nucleus to the point of rest is called the positron range, which for ^{18}F is around 0.1 mm. Positrons emitted from ^{18}F have an extremely short lifetime and annihilate with electrons from the surrounding tissue converting their total energy into electromagnetic energy, as seen in Fig. 1. Following the annihilation in this low-energy case, momentum conservation dictates that two gamma photons of equal energy of 511 keV are emitted in opposite directions (it should be noted that non-collinearity of 511 keV gamma rays can be up to $\pm 0.25°$ due to non-zero initial momentum[3]). Since positrons and electrons have the same mass, both annihilation photons have a characteristic energy of 511 keV. The two annihilation photons are emitted isotropically, meaning that the annihilation radiation from multiple annihilation events is emitted equally in all directions with the same intensity (ie: there is no preferential direction for the emission). This allows datasets to be collected with detectors that surround the area of radioactive distribution.
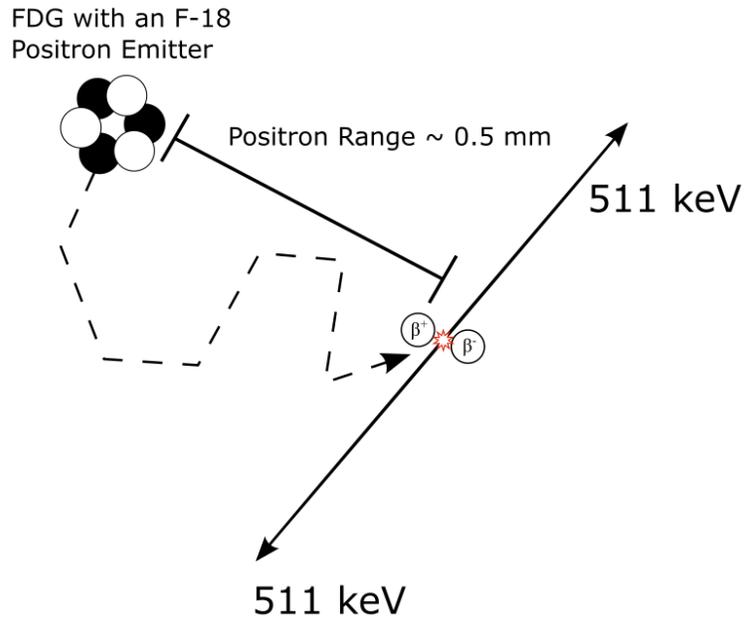
Fig. 1: A basic schematic showing the process of positron emission from a molecule labeled with ^{18}F, the positron scattering through a medium, positron-electron annihilation, and the emission of two antiparallel 511 keV photons.

Traditional PET scanners use a ring type detector which completely encompasses a patient's body so that the two antiparallel photons can be detected. These rings scan along the length of the body and record detected gamma photons at each location along the patient's body as it scans. Photons that are detected on opposite sides of the ring and are within a pre-set time frame of each other, called the "coincidence time window", are recorded as a coincident event and are used in the reconstruction of three-dimensional (3D) images of the radioactive distribution. The two detections are connected in an image space as the endpoints of a line called a "line of response" or LOR, along which the point of annihilation must be located. LORs are projected in the image space, and the points of intersection between the LORs within this space describe the location of radioactive emissions. An increased number of intersections are represented as increased contrast or brightness in the image and correspond to a higher emission rate and thus a larger radiotracer uptake.

Coincident events are classified into four categories based on the different ways that the annihilation photons can be affected: true coincidences, random coincidences, scattered coincidences, and multiple coincidences (Fig. *2*). True coincidences have an LOR which correctly passes through the location where the positron-electron annihilation occurred and are ideally the only events that should be considered during image reconstructions. Random coincidences involve two separate emissions which register a single photon from each pair of annihilations, within the coincidence time window, and incorrectly assigns the LOR between the two. These events are difficult to filter out since they are indistinguishable from a true coincidence, thus they typically become included in the dataset that is reconstructed adding to the image noise. Scattered coincidences involve the scattering of one or both of the 511 keV photons resulting in an assigned LOR that has deviated from its original true path. A scattered coincidence has a shifted LOR that no longer passes through the site of annihilation and thus incorrectly assigns radioactivity to a location that did not emit the photon pair. Since scattered photons lose some of their energy during the scattering process, these events can be filtered out based on placing a condition (cut) on the recorded energy from each detection. Although theoretically, for each single scattering coincidence, a scattering angle can be determined by the recorded energy of the detected photons, and then possible locations of scattering can be calculated based on the scattering angle, this analysis is not conventionally applied in practical PET systems and as such, scattered photons which are not filtered contribute to image blur deteriorating the image spatial resolution. Multiple coincidences occur when multiple annihilations happen in a timeframe that allows for the detection of three or more 511 keV photons within the coincidence window. With three or more detections

16

it is typically impossible to assign the LOR with 100% certainty, and as such these events are usually discarded.
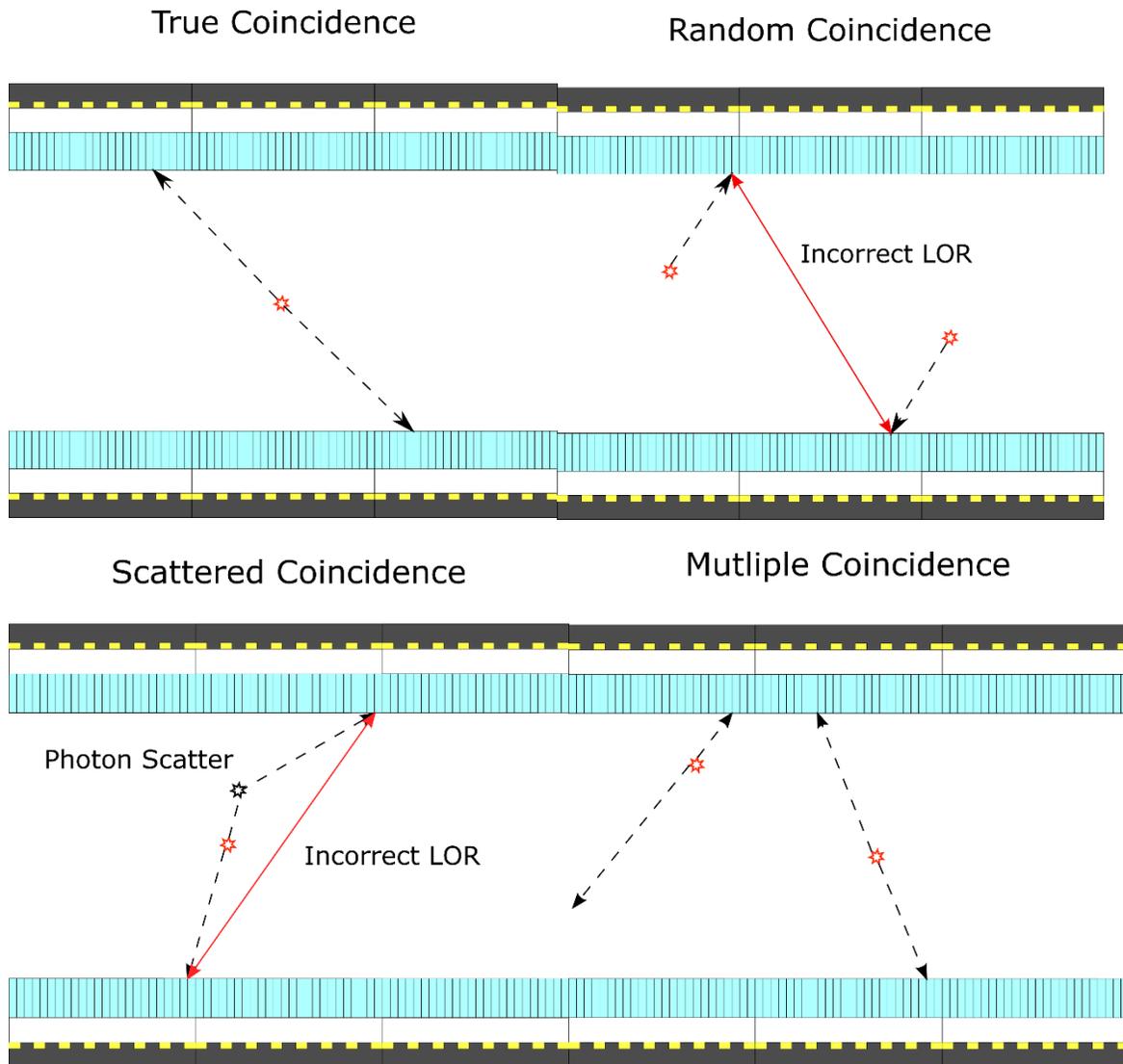
Fig. 2: Different types of coincident events: A true coincidence (Top, Left), Random Coincidence (Top, Right), Scattered Coincidence (Bottom, Left), and Multiple Coincidences (Bottom, Right).

1.2 Overview of Gamma Detectors for PET

To detect the high energy radiation involved in positron emission, detectors need to convert the emitted 511 keV photons into a usable electrical signal. Additionally, to accurately reconstruct

a 3D image, detectors must determine the location of each detection with a high degree of spatial accuracy. To achieve this, PET detectors are composed of an indirect conversion layout which consists of a high-density scintillation crystal optically coupled to high-gain photosensors.

Stopping such low-energy photons is achieved mainly through one of two photon-matter interactions: Compton scattering or photoelectric effects. In a photoelectric interaction an incident photon will transfer its entire energy to an orbital electron which will escape its parent atom with a kinetic energy equal to the incident photon energy minus the electron binding energy (1).

$$E_{k,pe} = E_{Ph} - E_B \tag{1}$$

Compton scattering of incident radiation occurs when the photon interacts with a loosely bound electron in the medium. This process will impart some of the photon energy to the scattered electron. The Compton photon after scattering will have a lowered energy and change its direction relative to the incident trajectory. Conservation of momentum and energy yields a straightforward relationship between the angle of scatter and the energy of a scattered photon with an initial energy of 511 keV (2).

$$E_{Scatter}(keV) = \frac{511\ (keV)}{2 - \cos\theta} \tag{2}$$

Through the above-mentioned interactions, scintillation crystals convert incident radiation into detectable optical signals: in indirect conversion detectors, which contain an intermediate step between the impinging gamma rays and photodetection, specially engineered crystalline scintillator materials are used.

Scintillation crystals are a wide band-gap crystalline material that, when irradiated with photons, act as a medium that emits visible light as energy is deposited in the crystal either by

18

Compton scatter or by photoelectric absorption. As the primary electron passes through the scintillator, it loses energy and excites other electrons across the band gap creating secondary electron-hole pairs. As is shown in Fig. 3, a majority of scintillators are doped to create activator energy levels. The excited electrons are trapped there and then decay back to their ground state, emitting a monochromatic photon as they do so.

The amount of light emitted from a scintillator is proportional to the amount of energy that is deposited into the material. The integrated light signal from the scintillator is converted by a subsequent photon detector from photons to electrons, therefore the scintillator brightness (the number of light photons produced per interaction of 511 keV) is one of the main characteristics of a scintillator which determines its efficiency. Other important characteristics which should be considered in choosing a scintillator for a particular application are the scintillator's stopping power, the wavelength of the emitted light, and the time over which the light is produced – the decay time. Also, for the purposes of PET imaging, the scintillator must be a dense material that can stop a large fraction of the incident 511-keV photons. Table 1 compares between the properties of selected scintillation crystals that are candidates for PET.

It is preferred for scintillators to have a high proportion of photoelectric interactions over Compton interactions. This is because all incident photon energy can be transferred to a photoelectron, effectively depositing the total energy into the crystal all at once. This type of effect is easily controlled and has a high degree of certainty for event assignment. Conversely, Compton effects have the possibility of scattering an incident photon outside of the detector resulting in missed or incorrect detections. Photoelectric effects are less likely to occur as incident photon

energy increases, so scintillators must be engineered to maximize the probability of photoelectric interactions.

Table 1: Comparison between the properties of selected scintillation crystals that are candidates for PET.

Property	Characteristic	Desired Value	LuYAP:Ce	BGO	LYSO	NaI
Density (g/cc)	Defines detection efficiency	High	7.2±0.2	7.1	7.4	3.7
Decay time (ns)	Defines detector dead time and random rejection	Low	20	300	40	230
Light yield (photons/keV)	Influences energy and spatial resolution	High	12	9	30	38
Peak emission (nm)	Defines the photosensor in use	Matched to photosensor	320-350	480	420	410
Ratio between photoelectric and Compton %	Influences accuracy of event assignment, energy, and spatial resolution	High	N/A	78	33	18

Typical scintillators in use for PET have a light output on the order of 10,000 photons per 511 keV photon. This light is emitted isotropically within the crystal and needs to be directed towards the photodetectors. The surfaces of each pixelated crystal element are coated with an enhanced spectral reflector (ESR) so that the scintillation light can only escape a given crystal element on one of its sides. The side without a reflective coating is mounted to a light guide, which then distributes the scintillation light over the array of photodetectors Fig. 4. Allowing scintillation light to distribute (mix) itself through the light guide means that multiple photodetectors will register signals from a single crystal pixel. After the total signal is registered, a method for

20

calculating the center of gravity of the light distribution allows for the determination of the crystal element that produced the response.
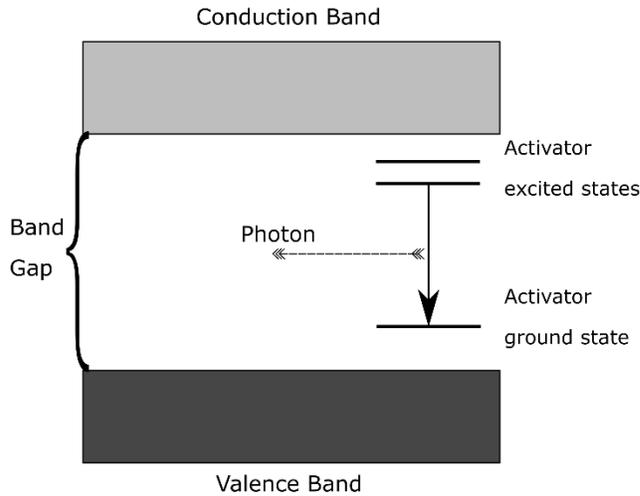
Fig. 3: Schematic of a scintillator band gap with doped activator energy levels.

Calculation of the center of gravity for the light through the light-guide is performed by measuring the sum of the signals along the rows and columns of the photodetectors. Taking a weighted difference between either the columns or rows and normalizing to the total signal gives the location of the center of the distribution along that direction. This type of calculation is called an Anger logic[4] and can be applied to an arbitrary number of columns or rows of detectors. Applying this calculation to both directions gives the coordinate along the X and Y directions of the detector module where the gamma impact occurred (3). Along with positional information, the total sum of the photosensor signal is related to the number of scintillation photons produced, which is proportional to the amount of energy deposited in the crystal. In this way, the energy from each gamma photon can be determined and recorded for event energy filtration to reduce the contribution of scattered photons and to improve image resolution.
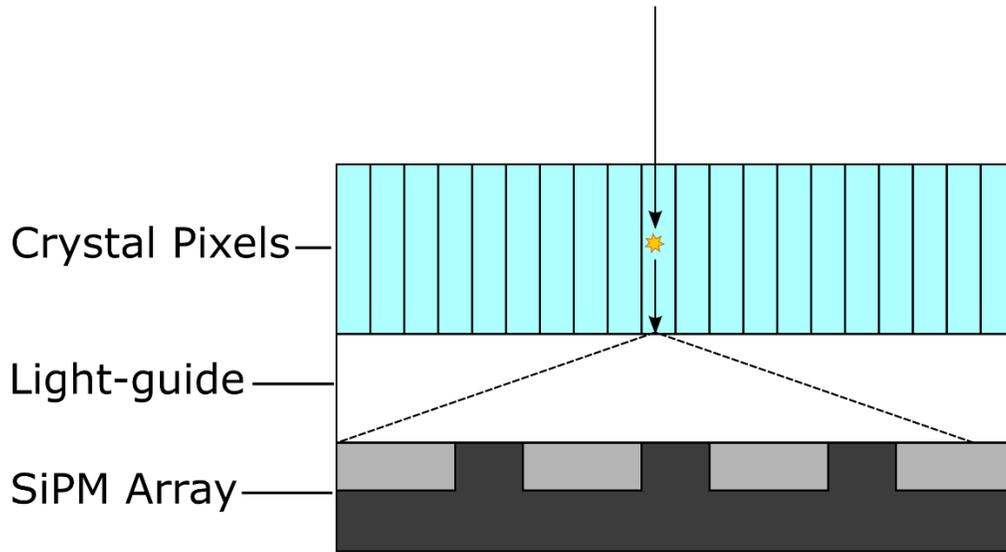
Fig. 4: Schematic representation of the scintillation light distribution through the lightguide of a SiPM detector module.

$$X_{Pos} = \frac{X^+ - X^-}{X^+ + X^-} \; ; \; Y_{Pos} = \frac{Y^+ - Y^-}{Y^+ + Y^-} \tag{3}$$

Photodetector elements in PET are required to have a high-signal gain to measure the low-energy scintillation light that is emitted. Ideally, the maximum of the photodetector quantum efficiency must correspond to the peak emission from the scintillator. Additionally, PET photosensors need to have a fast signal response to register all the ~10,000 photons that are emitted from a crystal without introducing any significant dead time. Thus, the photosensor of choice for older generations of PET has been the analogue Photomultiplier Tubes (PMTs), which dominated applications in medical and particle physics for over seven decades. Light from the scintillator is transmitted through the glass entrance window of the PMT and excites the photocathode to liberate an electron. A high-potential difference accelerates the electron liberated from the photocathode

22

and directs it to a series (normally 10) of positively charged dynodes. Between the collision with the dynodes each impinging electron acquires sufficient energy to release on the order of 3 to 4 secondary electrons from each dynode, thus creating an avalanche of photoelectrons with the overall multiplication gain of $\sim 10^6$ giving a current response within the milliamp range.

The use of PMTs as the photosensor of choice for PET detectors is quickly becoming antiquated due to the emergence of solid-state photosensors in the form of pixelated Silicon Photomultipliers (SiPMs). SiPMs are a high gain photosensor similar to PMTs with a signal gain of $\sim 10^6$ and a fast signal rise time. Each SiPM consists of several thousands of microcells, each of which acts as an avalanche photodiode, joined on a common substrate with common signal output and working on a common load. The high-signal gain of SiPMs is due to an avalanche multiplication process within the semiconductor whereby photogenerated charge carriers are accelerated through an applied electrical reverse bias. The reverse bias is large enough for the photodiode elements to operate in "Geiger mode"[5] (Fig. *5*) (i.e.: with a voltage larger than the breakdown voltage of the photodiode). Upon accruing energy during acceleration, both types of carriers will undergo impact ionization creating secondary electron-hole pairs. As such, a self-sustaining avalanche process is initiated resulting in the generation of a huge number of charge carriers, which are swept through the structure by the applied field.

Geiger micro-cells are all interconnected in parallel through their individual current limiting (or quenching) resistors to a common electrode. The quenching resistor is needed to control the overall gain: as the field in the multiplication layer collapses due to the voltage drop on the quenching resistor, the acceleration of free carriers is brought to an end and the avalanche is quenched. The total number of free carriers generated in an avalanche defines the total gain, which

23

is proportional to the overvoltage $\Delta V = V_{bias} - V_{br}$, where V_{br} is the breakdown threshold voltage. However, since the current through the bulk of Si grows to the value limited by the quenching resistance, the gain is fixed by the external circuit, not by the statistics of the impact-ionization process. This results in stable and reproducible gain. Once the photocurrent is quenched the photodiode can recharge to its regular operating state and allow for additional avalanches to occur.
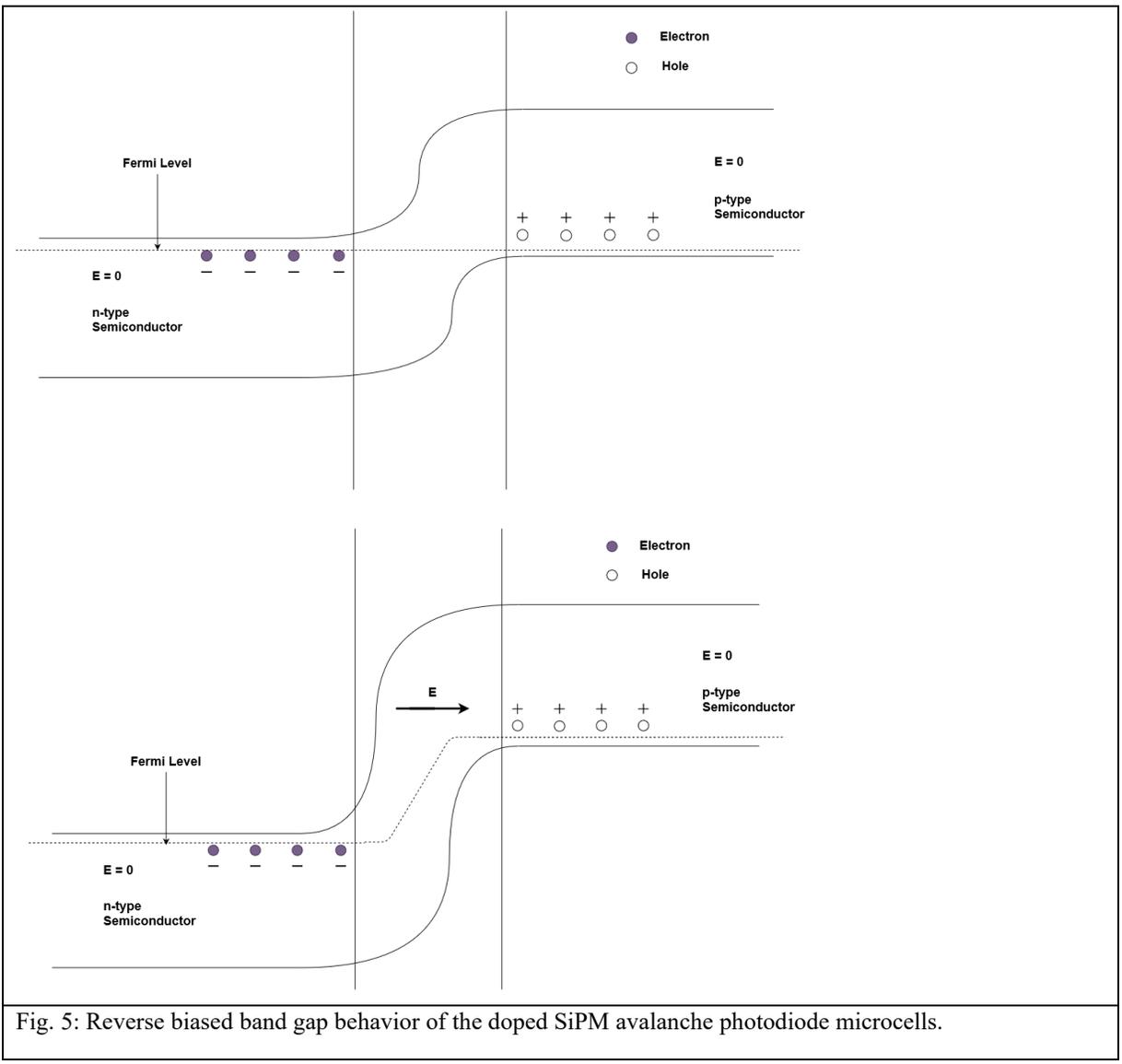
Fig. 5: Reverse biased band gap behavior of the doped SiPM avalanche photodiode microcells.

SiPMs have the benefit of being small compared to PMTs with pixels as small as 1 mm^2, have low operating voltage[6,7] and are insensitive to magnetic fields, the latter point being an important distinction for the use of PET in conjunction with MRI (a task that is impossible with the use of PMTs). Additionally, SiPMs have been shown to be well suited for application to time-of-flight (TOF) PET where the precise timestamp of each recorded detection is required. Thus, given the inherent benefits of using SiPMs over PMTs, modern generation PET detectors have begun implementing these photosensors in the design of new PET cameras including WB PET, Total Body PET, PET/MRI, and brain dedicated systems[8–12]. In addition, SiPMs allow for an innovation in the design of the detectors, whereby the modules can be tiled together resulting in a large area flat panel PET detector with a low profile. The compactness that is achieved is important for building slim detector heads, which minimizes the distance between the FOV and patient's body, for an improved detectability of deep-chest lesions[13]. An increase in the size of the detector arrangement and the seamless edges between individual modules can significantly increase the sensitivity of the camera. The increase in sensitivity is mainly due to two factors: 1) an increase in the packing fraction of the detector modules which improves the collection efficiency from a reduction of dead-space, and 2) a larger solid angle coverage because of the continuous, active, sensor area in close proximity to the organ in question. A lack of the use of SiPM detectors in breast-targeted PET[14,15], as well as the inherent improvements that organ-targeted imaging can offer, has inspired the design of the PET camera which is investigated below.

1.3   PET System Design and Implementation

Organ-targeted PET has enormous potential for new advances in diagnosis and theranostic applications across a wide clinical spectrum, from cancer to cardiac and neuroimaging. Downscaling a PET system to an organ targeted PET camera has benefits based on the improvements that can be achieved with smaller detectors placed closer to the region of interest. Smaller detector elements improve spatial resolution, and cameras that are designed to improve the solid angle coverage of the organ will increase the collection efficiency of radioactive sources within the FOV. Because of these improvements, organ targeted PET is needed as an alternative to WB PET technology for new precise examinations due to its high sensitivity, high spatial resolution, and high signal-to-noise ratio. However, there are barriers to its widespread adoption in clinical practice. The systemic injection of radiopharmaceuticals into the patient makes the problem of radiation exposure one of the critical issues associated with PET imaging. New approaches to maximize PET detector sensitivity are needed to reduce the effective dose associated with organ-targeted PET imaging. This will significantly expand patient populations for whom PET is an appropriate imaging modality, especially in diagnosis.

One of the leading applications for organ-targeted PET is breast cancer, where molecular breast imaging can address existing limitations in X-ray mammography related to dense breasts[16] and in MRI related to specificity[17] and hormonal variability in breast tissue[18]. In particular, breast-targeted PET cameras could be useful in assessing the metabolic activity of primary lesions for treatment planning and evaluating treatment response[19].

The clinical prototype organ-targeted PET system developed through Radialis Medical has an array of block detectors constructed with SiPM photodetectors coupled to arrays of LYSO

26

scintillation crystals by a specially designed light-guide (Fig. 6, Fig. 7). The design allows for a seamless array of detectors to be placed next to each other, resulting in a large area detection surface which is modular in nature and can be tiled together into any configuration. The specific layout of detector modules for each detector head of the camera is a 4×3 array with each module being 57.52 × 57.52 mm^2 in size meaning the total active area of the detector surface is 230.64 × 172.98 mm^2.
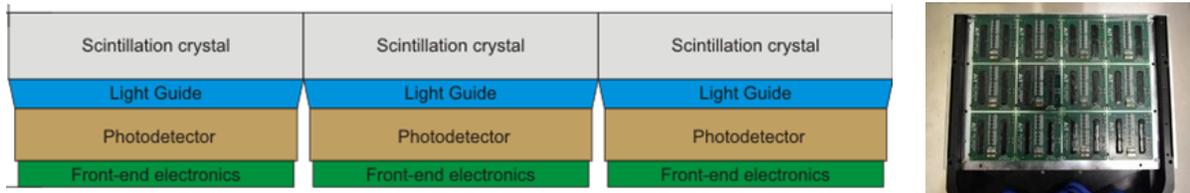
Fig. 6: Left: Schematic presentation of the cross-section of three tiled detector blocks; Right: top view of 3×4 array of sensor modules inside a detector head.
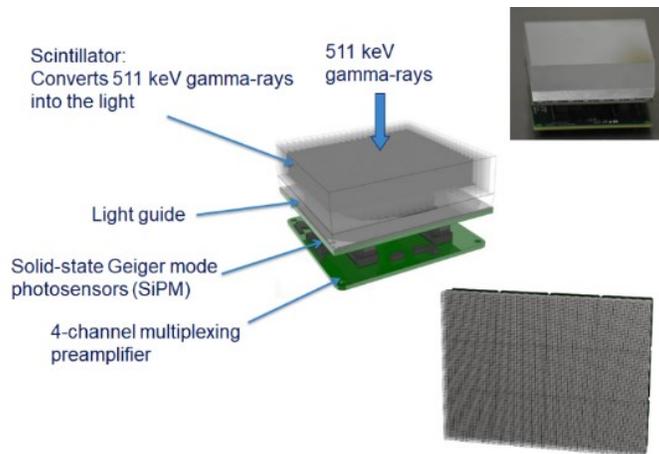
Fig. 7: Single detector module design showing the arrangement of scintillation crystal on top of the light guide and photosensors.

The scintillation material used for the detector modules is a Cerium doped Lutetium-Yttrium Oxyorthosilicate (LYSO) crystal which is manufactured into a pixelated matrix of rectangular crystals covering the entire active area of each module. The pixel size of these crystal matrices is

27

$2.32 \times 2.32 \times 13$ mm^3 with a crystal pitch of 2.4 mm. The total size of the 2D array of crystals is 24×24 and a single matrix size is 57.6×57.6 mm^2. It is important to note that this crystal contains Lutetium which contains 2.6% of the isotope ^{176}Lu and is itself radioactive. This can contribute to a small number of false events detected due to the intrinsic radioactivity of the detectors themselves. False coincidences are minimized by choosing a timing window which minimizes most randomly injected counts. These events, when included in acquisition datasets, decrease the image SNR by increasing the background counts. False coincidences do not assign LORs to a true detected event within the FOV and thus must be minimized by a narrow coincidence window.

LYSO scintillation crystals that are 13 mm thick have an absorption efficiency of between 60% to 70% for 511 keV photons Fig. 8. This means that for the measurement of a coincidence between two crystals, the maximum counting efficiency that is achievable with those crystals is between 36% and 49% for the impinging gamma rays. For a PET detector arrangement, the additional losses to count rate efficiency come from the solid angle coverage of the FOV being less than 4π steradians. The overall sensitivity composed of geometric effects and detector efficiencies is presented in (4).
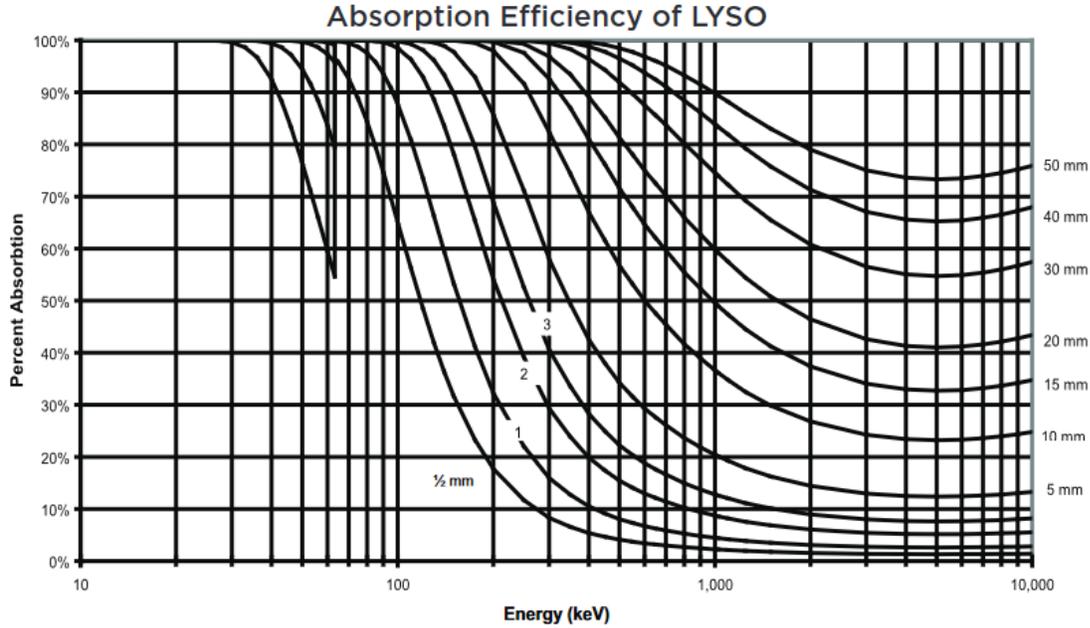
Fig. 8: Absorption efficiency for LYSO crystals with varying thicknesses.
Source: https://www.crystals.saint-gobain.com/sites/imdf.crystals.com/files/documents/lyso-material-data-sheet.pdf

$$\eta = 100 \times \frac{\varepsilon^2 \varphi \Omega}{4\pi} \tag{4}$$

The overall system sensitivity η consists of a composition of the detection efficiency ε which is squared to account for the detection of an event on both detectors (necessary for a coincidence event), the packing fraction φ of the detector being used (i.e.: how much of the detector surface is an active detector area), and the geometric efficiency of the system Ω which is characterized by the solid angle coverage of the detectors with respect to the radioactive source within the FOV.

The photodetector in use is a Silicon Photomultiplier (SiPM) array developed by ON Semiconductor[i] (Phoenix, Arizona) called "ArrayC" SiPMs. These SiPMs are a pixelated array of detectors (8×8) which consist of 19,000 microcells, each of which acts as an individual avalanche

---

[i] ON Seminconductor is now called onsemi (https://www.onsemi.com)

29

photodiode. Some of the primary characteristics of ArrayC are tabulated in Table *2*. This array of SiPMs has a 16-channel multiplexing readout which is reduced to 4 channels by the pre-amplifier.

Table 2: Characteristics of the "ArrayC" SiPMs developed by ON Semiconductor.

Parameter	ArrayC
Number of SiPM pixels	8x8
Pixel active area	6x6 mm^2
Pixel pitch	7.2 mm
Breakdown Voltage (V_{br})	24.5 V
Operating Voltage	30.5-31.5 V
Max Overvoltage	5 V
Peak Wavelength	420 nm
PDE for peak wavelength at +5 V_{br}	41 %
PDE for peak wavelength at +2.5 V_{br}	31 %
Microcell recovery time	95 ns
Temperature dependence of V_{br}	21.5 mV/°C

Since this design uses a FOV which covers the entire axial extent of the organ in question, the overall system sensitivity should be relatively high. To validate improvements to the overall system sensitivity of such a device, experimental investigations based on standardized methods are required. In addition to this, the spatial resolution and system count rates also defined by standardized experimental evaluations can quantify the performance for this implementation of organ-targeted PET. These tests are outlined in more detail in the following chapter.

1.4 Standardized Evaluation Methods

PET systems can be quantitatively evaluated through multiple experimental tests, all of which have been standardized with documentation put forth by the National Electrical Manufacturers

Association (NEMA). The primary goal of these tests is to produce a set of results which characterizes the performance of a PET device and can be used to compare between different system designs. Measurements for spatial resolution, system count rates, sensitivity, and various image quality metrics are all defined for WB PET systems in the "NEMA NU 2-2018 Performance Measurements of Positron Emission Tomographs" and for pre-clinical PET scanners in the "NEMA NU 4-2008 performance measurements of Small Animal Positron Emission Tomographs". For organ-targeted PET systems, which have a reduced FOV, the experimental methods for WB PET systems in NEMA NU 2 are incompatible. Because of this, the standardized evaluation methods for this organ-targeted system follows the outlines for evaluating small animal PET systems in NEMA NU 4 and is described in detail below.

Spatial resolution is a system characteristic that represents the ability of the scanner to distinguish between closely positioned point sources. It is defined as the Full Width at Half-Maximum (FWHM) and Full Width at Tenth-Maximum (FWTM) of the reconstructed images Point Spread Function (PSF) for a positron emitting point source.

Medical imaging systems have non-zero spatial resolutions, which means that the signal from a source in the FOV will tend to smear out across the image in all directions, leading to a reduction of contrast and image blur. To quantify this effect, NEMA NU 4 recommends that small animal systems use a positron-emitting point source with a size that is smaller than the estimated resolution of the scanner for acquisitions. A standard NEMA point source, a Na-22 point source imbedded in 1 cm × 1cm × 1cm acrylic cube, is required for this measurement. Additionally, a source holder is needed to mount the point source onto a moving stage for precise positioning.

NEMA NU 4 requires the measurement of spatial resolution in two directions – radial and tangential, guided by the cylindrical geometry of small-animal PET scanners. The developed Radialis PET camera uses two planar detectors, so the radial direction is chosen to be the X and Y plane and the tangential direction is measured as the Z axis of the camera. The source is sampled across the FOV in all three directions and image analysis of the resulting point-spread function (PSF) informs the spatial resolution at each location. Image voxel size must be chosen such that the PSF of the point source spans at least five pixels in order to accurately measure the FWHM. Based on this requirement the voxel size in the X and Y directions is chosen to be 0.2 mm and in the Z direction is 2.67 mm. The PSF can be modeled by fitting a Gaussian distribution to it and taking the FWHM and the FWTM of the fitted curve.

System count rates inform the event processing performance of the system detectors and electronics. The measured values of count losses and random coincidences specify the accuracy with which the system detects events from highly radioactive sources. For a consistent and comparable experimental technique, NEMA recommends the use of a "scatter phantom" which is a high-density polyethylene (0.98 g/cm^3) cylinder with a hollow bore through the long axis of the phantom Fig. 9. Imaging of this phantom is done with a high-concentration activity solution filling the bore and performed over several half-lives of the radioisotope. Each acquisition must be timed for the determination of count rates in the analysis. Since the activity is concealed within a high-density material and the source is linear, scattered coincidences and true coincidences can be determined within images by observing the location of the events with respect to the measured peak of the source. The result from this analysis has two specific objectives: 1) to measure the scatter fraction (SF) as the relative system sensitivity to scattered radiation, and 2) to measure the

32

effects of scattered and random coincidences on acquired datasets and identifying the dead-time limitations of the system at different levels of activity.

Fig. 9: Scatter phantom which is used in the determination of system count rates.

Data collection is performed with intervals that are more frequent than the half-life of the radionuclide (110 minutes for ^{18}F). Measurements are taken until the single event rate is equal to twice the single count rate of the intrinsic activity. The duration of each data acquisition is $T_{acq,j}$ and is less than one fourth of the half-life of ^{18}F.

Each acquisition is conducted such that there are at least 500,000 prompt counts in the dataset and such that the system dead-time count loss rates and random rates are below 1.0% of true rates.

The intrinsic true count rate R_{int} is measured with the phantom positioned in the FOV but without any activity filled in it. Data is collected so that at least 10,000 counts are recorded in each

slice using a Single Slice ReBinning (SSRB) method. The total number of coincident events in each slice is divided by the data collection time to calculate the intrinsic true event count rate.

Data processing is performed using 120 slices each 2 mm thick and perpendicular to the X axis. The acquired data files are processed using an SSRB image reconstruction technique[20]. This method involves the creation of a single image plane halfway between the detectors which is filled with pixel values equivalent to the number of LOR's passing through each pixel. The resulting image maintains the true number of image counts as pixel values which provides a method for determining image counts and count rates for each acquisition. LOR acceptance angle filtration (DXY) is implemented to reject events within the list-mode data based on the endpoints of each LOR. If the difference between the top and bottom detection endpoints is larger than a certain threshold (DXY< threshold), then the event is discarded from the analysis.

A profile of the scatter phantom was created by summing the SSRB image along the Y axis and plotting the summed X bin values. This "maximum intensity projection" was used to determine the counts of the whole image including the true and scatter counts as defined in the NEMA NU-4 standards.

All bin values farther than 8 mm from the edges of the phantom are set to zero. Linear interpolation is used to find the bin intensities at ±7 mm from the central maximum bin of the projection profile as shown in Fig. 10.
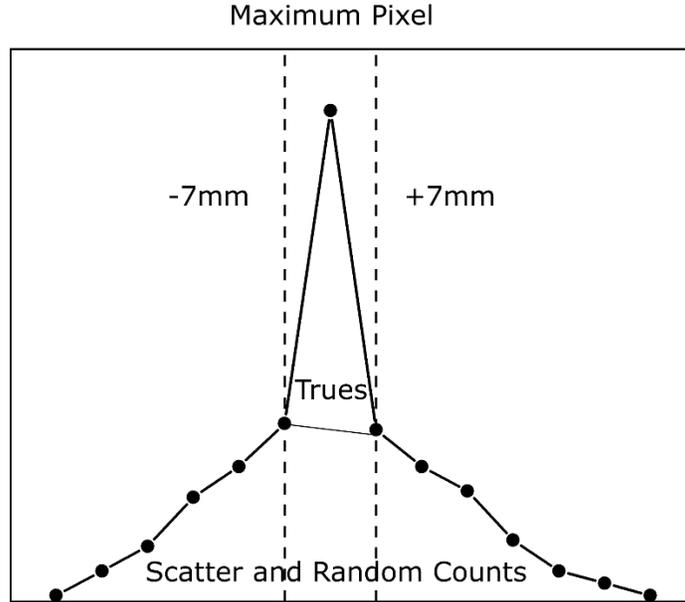
Fig. 10: Example sketch of the source peak and distribution that can be expected from the scatter phantom acquisition.

The average of the bin intensities at ± 7 mm are multiplied by the number of bins between them in the "trues" region, and the product is added to the counts outside of this region to get the number of scattered and random counts $C_{s+r,i,j}$ for each data acquisition. The total event count $C_{TOT,i,j}$ is calculated as the sum of all bin values in the sum projection for slice i of acquisition j.

The average activity $A_{ave,j}$ for each acquisition j is calculated as displayed in (5).

$$A_{aver,j} = \frac{A_0}{\ln 2}\left(\frac{T_{1/2}}{T_{acq,j}}\right)\left\{1 - \exp\left(\frac{-T_{acq,j}}{T_{1/2}}\ln 2\right)\right\} \tag{5}$$

Where A_0 is the initial activity at the beginning (T_0) of the acquisition and is calculated using the recorded A_{cal} dose calibrator activity at time T_{cal}. Thus, A_0 is calculated with (6):

$$A_0 = A_{cal}\exp\left(\frac{T_{cal} - T_0}{T_{1/2}}\ln 2\right) \tag{6}$$

The initial activity for acquisition j can be calculated with (7):

35

$$A_j = A_{cal}\exp\left(\frac{T_{cal} - T_j}{T_{1/2}}\ln 2\right) \tag{7}$$

For each slice i in each acquisition j, the total event rate $R_{TOT,i,j}$ is calculated as in (8).

$$R_{Tot,i,j} = \frac{C_{Tot,i,j}}{T_{acq,j}} \tag{8}$$

Where $T_{acq,j}$ is the acquisition time. The system total event rate $R_{TOT,j}$ is calculated as:

$$R_{Tot,j} = \sum_i R_{TOT,i,j} \tag{9}$$

True count rates for each timeframe can be determined by summing the counts beneath the source peak (Fig. 10) and subtracting the counts that are assumed to be random and scattered coincidences. This will yield only the coincident events that were correctly assigned to the source and are quantified as the system true counts (10).

$$R_{t,i,j} = \frac{C_{Tot,i,j} - C_{r+s,i,j}}{T_{acq,j}} \tag{10}$$

There are two measurements for system scatter fraction required for this analysis. The first is the scatter fraction of each slice defined in (11) and is used for the calculation of the random event rate (12).

$$SF_i = \frac{\sum_{j'} C_{r+s,i,j'}}{\sum_{j'} C_{TOT,i,j'}} \tag{11}$$

$$R_r = R_{Tot,i,j} - \left(\frac{R_{t,i,j}}{1 - SF_i}\right) \tag{12}$$

This value of scatter fraction is measured from the low-activity acquisitions. The system scatter fraction is computed at five times the amount of activity that produces the same number of

single event counts as the intrinsic activity and is defined for systems which employ detectors with intrinsic radioactivity as in (13). For detectors with materials that contain intrinsic radioactivity, the scatter fraction must be determined from the measured scatter event rate and true event rate.

$$SF_j = \frac{R_{s,j}}{R_{t,j} + R_{s,j}} \tag{13}$$

The scatter event rate in (14) first requires the determination of true event rate and random event rates, the latter of which needs the slice scatter fraction determined previously in (11).

$$R_{s,i,j} = R_{TOT,i,j} - R_{t,i,j} - R_{r,i,j} - R_{int} \tag{14}$$

The noise equivalent count rate (NECR) calculated with (15) is an estimate for the number of true coincidences acquired per second which is free from the effects of scattered and random coincidences and the intrinsic radioactivity of the system.

$$R_{NEC,i,j} = \frac{R_{t,i,j}^2}{R_{TOT,i,j}} \tag{15}$$

A standard NEMA NU 4 2008 Na-22 point source is required for the measurement of the system sensitivity. A source holder and stepper motor stage are used to position and move the source within the field of view Fig. 11.
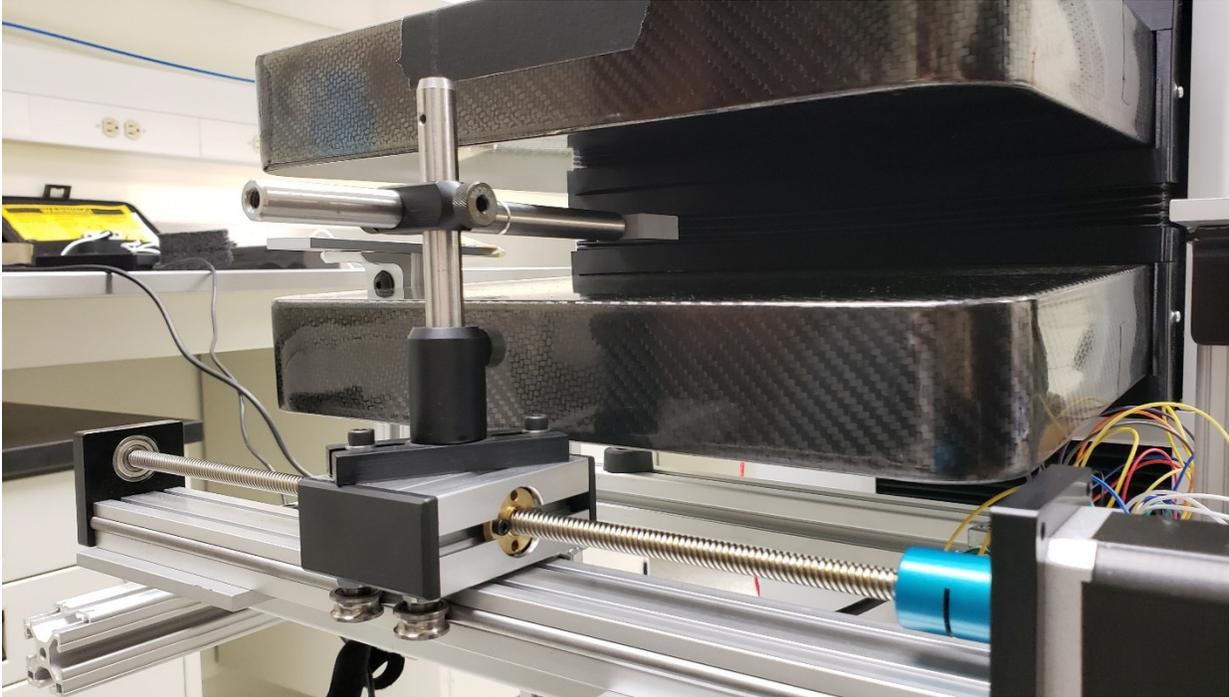
Fig. 11: Source holder and stepper motor stage used for positioning of the point source during sensitivity and spatial resolution acquisitions.

The procedure for total and absolute sensitivity measurement follows the NEMA NU 4 2008 specifications and, while not part of the NEMA NU 4 2008 standard, normalized sensitivity is calculated by dividing the sensitivity values by the total number of slices used. This procedure was previously reported for the performance assessment of the PEM Flex Solo II[15]. In this measurement set, the detector heads are placed 60 mm apart.

For the sensitivity measurement the activity of the Na-22 point source is measured in a dose calibrator and recorded as A_{cal}. The source is placed in the center of the field-of-view such that it is centered both in axial and transaxial directions.

Data is acquired for 10,000 events and the time duration for this acquisition is recorded as T_{acq}. The source is moved in steps towards the end of the axial field-of-view in the X direction. The count rate R_i is determined by dividing the number of events by the acquisition time $T_{acq,i}$. The

38

background true event rates $R_{B,i}$ are determined by acquiring a dataset with no source in the field of view, for a duration equal to $T_{acq,i}$. Upon reaching the edge of the FOV, the source is returned to the center of field-of-view and the same procedure is repeated with the steps in the opposite direction.

The step size is governed by the thickness of the slices perpendicular to the direction of the source movement. It is chosen to have 120 slices each with thickness of 2 mm. SSRB is used to assign the events with oblique LORs to the image slice where the LOR crosses the scanner axis. No other corrections for scattered or random events are performed. Per NEMA NU 4 no decay correction is performed in as much as the duration of the test is significantly shorter than the 2.6 year half-life of the Na-22 source.

The per-slice sensitivity is calculated with (16), where the count rate for that slice R_i is normalized to the measured activity of the source $A_{Cal,}$ and has units of counts per second per Becquerel (cps/Bq). The peak per-slice sensitivity is measured in the center of the FOV and is what is typically used to compare between different PET cameras for the maximum achievable sensitivity.

$$S_i = \frac{R_i - R_{B,i}}{A_{Cal}} \tag{16}$$

Absolute per-slice sensitivity is a unitless percentage which incorporates the branching ratio of ^{22}Na (0.9060) and is specified by (17).

$$S_{A,i} = \frac{S_i}{0.9060} \times 100 \tag{17}$$

The quantification of the above-mentioned performance metrics for PET cameras informs not only the comprehensive performance of the system but also indirectly of the performance of the

39

composite systems (detectors and coincident signal processing electronics). The clinical viability of this prototype device can be inferred from how these system performance tests compare to other systems tested with these standardized experiments. The clinical capabilities of the organ-targeted PET camera can also be derived based on the results of these tests. Thus, the results presented here are important for the investigation of the implementation of organ-targeted PET cameras as well as providing significant value for the argument to integrate organ-targeted PET into clinical protocols.

2 Section 2 – Evaluation of the High-Sensitivity Organ-Targeted PET Camera

The following contains the content from the publication: J. Stiles, O. Bubon, H. Poladyan, B. Baldassi, V. Freitas, A. Scaranelo, M. Waterston, A. Reznik, "Evaluation of a High-Sensitivity Organ-Targeted PET Camera" which is submitted to the journal: Medical Physics.

The full text from the manuscript of this article is included below.

Evaluation of a High-Sensitivity Organ-Targeted PET Camera

Justin Stiles[1*], Oleksandr Bubon[1,2], Harutyun Poladyan[3], Brandon Baldassi[1], Vivianne Freitas[4,5], Anabel Scaranelo[4,5], Michael Waterston[2], Alla Reznik[1]

1 - Lakehead University, Thunder Bay, Canada

2 – Radialis Medical, Thunder Bay, Canada

3 – Thunder Bay Regional Health Research Institute, Thunder Bay, Canada

4 - University Health Network, Sinai Health System, Women's College Hospital, Toronto, Canada

5 - University of Toronto, Toronto, Canada

2.1 Abstract

Purpose: The aim of this study is to evaluate the performance of the Radialis organ-targeted positron emission tomography (PET) camera with standardized tests and in a clinical setting in comparison with other imaging modalities.

Methods: Sensitivity, count rate performance, and spatial resolution were evaluated according to the National Electrical Manufacturers Association (NEMA) NU-4 standards, with necessary modifications to accommodate the planar detector design. The detectability of small objects was demonstrated with Micro hotspot phantom images. The clinical performance of the camera is also showcased through the acquisition of breast cancer images with varying injected doses of 2-[fluorine-18]-fluoro-2-deoxy-D-glucose (^{18}F-FDG) and comparison to digital full-field mammography, magnetic resonance imaging (MRI), and whole-body (WB) PET imaging.

Results: Spatial resolution was calculated to be (2.3 ± 0.1) mm for the in-plane resolution and (6.8 ± 0.1) mm for the cross-plane resolution using maximum-likelihood expectation maximization

42

(MLEM) reconstruction. The system peak noise equivalent count rate was 17.8 kcps at a ^{18}F-FDG concentration of 10.5 kBq/mL. System scatter fraction was 24%. The overall efficiency at the peak noise equivalent count rate was 5,400 cps/MBq. The maximum per-slice sensitivity achieved was 3.5%, with a system normalized sensitivity of 2.4%. Micro hotspot phantom sources were visualized down to 1.35 mm diameter rods. Selected results from clinical trials demonstrate capability to image lesions at the chest wall, identify false-negative X-ray findings, and false-positive MRI findings, even at up to a 10-fold dose reduction in comparison with standard ^{18}F-FDG doses (i.e., at 37 MBq or 1 mCi).

Conclusion: The evaluation of the organ-targeted Radialis PET camera indicates that it is a promising technology for high resolution low-dose PET imaging. High-efficiency radiotracer detection makes it possible to reduce administrated doses of radiopharmaceuticals and, therefore, patient exposures to radiation.

2.2   Introduction

The emergence of new radiotracers for positron emission tomography (PET) is continuing to expand its impact on clinical practice. The development of new precision radiotracers binds imaging activity to specific clinical targets advancing personalized (or precision) medicine[21]. In addition to scanning of the body with whole-body (WB) PET scanners, the applications for PET imaging increasingly involve the visualization of specific organs[22]. Compared to WB PET scanners, an organ-targeted PET system is capable of higher efficiency, higher spatial resolution and higher signal-to-noise ratio resulting in better image contrast and enabling more precise PET examinations. Indeed, an organ-targeted PET camera with optimized geometry can position detectors in close proximity to the organ of interest to facilitate 1) more efficient gamma-ray

43

detection; 2) higher spatial resolution; and 3) reduced unwanted signal from elsewhere in the body, improving the noise equivalent count rate (NECR) within the field of view (FOV) due to a reduction of false coincidences.

Although organ-targeted PET has the potential for new advances in diagnosis and theranostic procedures across a wide clinical spectrum, from cancer to cardiac and neuroimaging[23], the adoption in clinical practice has been limited by the relatively high exposure to systemic radiation and organ-specific limitations in applications[24–27]. New approaches to maximize PET detector sensitivity are needed to reduce the effective dose associated with organ-targeted PET imaging. This will significantly expand patient populations for whom PET is an appropriate imaging modality, especially in diagnosis. In addition, organ-targeted PET technologies are primarily limited to a single target organ, which can pose challenges for maintaining high utilization rates[24].

The above problems are addressed in this publication: we report on the Radialis PET camera that is a versatile, high-sensitivity solid-state PET camera developed at Lakehead University and manufactured by Radialis Medical in Thunder Bay, Canada for low-dose organ-targeted imaging.

The Radialis PET Camera is evaluated in terms of the activity sensitivity, system count rates, and spatial resolution[28–30] and is compared to other commercially available systems. In addition, selected results from a clinical study in progress at the University Health Network – Princes Margaret Cancer Centre, Toronto, Canada to evaluate the performance of the Radialis PET Camera with low radiotracer (i.e., 2-[fluorine-18]-fluoro-2-deoxy-D-glucose (^{18}F-FDG)) activity are presented. The field-of-view and detector configuration in the Radialis PET Camera has been used

44

for imaging of the heart, brain, and breast. Here we present imaging results with breast cancer patients.

2.3   Materials and Methods

The Radialis PET Camera employs two planar detector heads (Fig. 12) each containing 12 four-sided tileable (mosaic) sensor modules that are arranged against each other (Fig. *13*, left) to assemble a uniform planar sensing area.

Each sensor module uses an advanced scintillation crystal, Cerium doped Lutetium Yttrium Orthosilicate (LYSO), in combination with a matching array of SiPMs (the Array-C 8 × 8 array of SiPMs developed by ON Semiconductor (Phoenix, Arizona)). The scintillation crystal is pixelated to make a 24 × 24 crystal array with a pixel size of 2.32 mm × 2.32 mm × 13 mm. LYSO and SiPMs are optically coupled through uncoated 5 mm thick Borosilicate light guide that allows the light to be spread over multiple SiPM pixels for the use of coordinate reconstruction methods that rely on light sharing techniques. Also, the light guide has slightly slanted edges so that the front face and the back face of the light guide have the exact dimensions of the scintillating crystal array and the photodetector layer, respectively[28]. As can be seen from Fig. 13, all the modules' components and front-end electronics are mounted in such a way that none of the components is larger than the scintillating crystal. As a result, the scintillating crystal has an overhang over the photosensor array to maintain full tileability so that sensor modules can be seamlessly combined into a sensor area of the needed size.

The detector architecture relies on multiplexed readout: 64 channels of the SiPM array in each sensor module are multiplexed to 4 readout signals from the pre-amplifiers (AiT AB4T-

45

ARRAY64P). Event coordinates are reconstructed from this 4-channel signal readout which is applied to an Anger Logic[4] to determine the coordinate of each detected event. Lines of response (LORs) are collected and stored in list-mode format for the reconstruction of an image of the radiotracer distribution by an iterative maximum likelihood expectation maximization (MLEM) method[31]. A median root prior filter[32] is applied within the MLEM reconstruction after each iteration.

The timing and energy windows for image acquisitions are set at 4 ns and 350-700 keV respectively and are consistent through each acquisition. The energy window is kept relatively wide to allow for a higher sensitivity for low activity imaging.

Fig. 12: Configuration of the Radialis PET Camera with two planar detector heads to be positioned on either side of a breast.

In addition to the energy window filter for each event, a LOR angle allowance filter is implemented to reject events within the list-mode data based on the endpoints of each LOR. If the difference between the top and bottom detection endpoints is larger than a certain threshold, then the event is discarded from further processing. This discriminates oblique LORs and thus reduces the contribution of parallax effect; however, this reduces sensitivity.

Fig. 14 shows how the sensor modules are arranged in a 3×4 array inside a detector head of the Radialis PET camera. The size of individual sensor modules shown in Fig. 13 (right) is 57.66 mm × 57.66 mm, which results in a seamless sensor area of 230.64 mm × 172.98 mm. The detector

housing is made from a thin, durable material so that the imaging area is only ~4 mm from the edge of the detector housing.

Thermal stability of the SiPMs is achieved by actively cooling the detector arrays using the built-in temperature control unit and maintaining the operating temperature of the detector head at (18 ± 1) °C[28]. This cooling approach allows for the stable operation of the detector heads during image acquisition in clinical setting.

In the design shown in Fig. 12, the adjustable separation and rotation of the detector heads allows for imaging a range of organs including the breast, axilla, heart, and prostate. Breast images are acquired in a seated position of patients with the detector heads placed on either side of the immobilized breast. The position of the detector heads and the distance between them is adjusted according to the patient's height and breast size. A gantry with a rotation axis allows for 90-degree rotation of the detector heads clockwise and counter-clockwise from its starting position which is needed to acquire breast and axilla images at standard views (i.e., bilateral craniocaudal (CC) and mediolateral oblique (MLO) views) as well as at supplementary views if additional information is required.
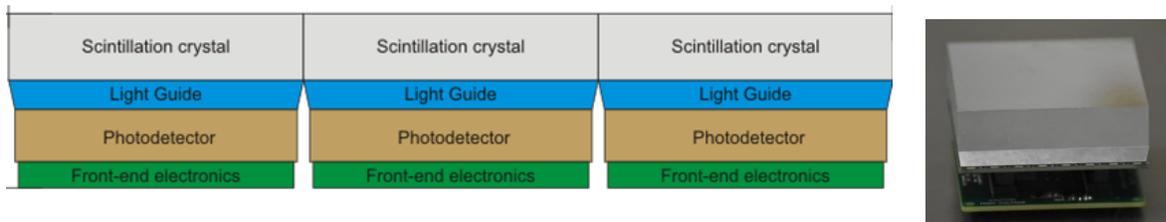
Fig. 13: Left: Schematic presentation of the cross-section of three tiled detector blocks; Right: The photo of a block detector with crystal array wrapped in a light reflective material and an electronic board underneath.

For imaging the heart, the detector heads are turned vertically and positioned on both sides of patient's chest in a seated position, while for prostate imaging the detector heads are placed above and below the pelvis of the patient lying on the patient bed (not shown in Fig. 12).

Fig. 14: Top view of 3×4 array of sensor modules inside a detector head.

Since there is no National Electrical Manufacturers Association (NEMA) standard designed for organ-targeted PET systems, the performance of Radialis PET was evaluated with the NEMA NU-4 2008 standards[33] for pre-clinical scanners. Indeed, the NEMA NU-4 2008 standards designed for small-size ring detectors are more appropriate to the Radialis PET camera than the NEMA NU-2 standards for WB PET/CT (Computed Tomography) scanners (the FOV of organ-targeted PET cannot accommodate the large phantoms required for NEMA NU-2). Tests of detector performance are conducted with the aim of determining spatial resolution; total, true, scattered, random, and noise-equivalent count rates; evaluation of system sensitivity; and evaluation of image quality.

It should be noted that the coordinate system defined by the NEMA NU-4 protocol assumes a ring geometry of small-animal PET scanners and refer to axial or transaxial directions for measurements of spatial resolution. However, the planar geometry of the Radialis PET camera is described in Cartesian coordinates shown in Fig. 15 with XY plane parallel to the detector heads and Z axis which points from one detector head to the other. A single slice re-binning (SSRB) reconstruction method[20] was used to process corrected list mode data according to sections 4 and 5 of the NEMA NU-4 - 2008 standards. This method assigns each line of response to an image plane halfway between the detector heads based upon the intersection of the LOR with the plane.

48

Also, the NEMA NU-4 - 2008 standard mandates derivation of spatial resolution through reconstruction of point -source images using a Filtered Back Projection (FBP) technique. This is a significant limitation since the majority of modern PET systems use an iterative MLEM reconstruction, so NEMA evaluation using FBP may not reflect the actual spatial resolution of the system[34]. Therefore, selected acquisitions for spatial resolution measurements are reconstructed using NEMA-specified back projection to directly follow the outlines in NEMA NU-4 – 2008 and are supplied with corresponding images done with MLEM to reflect the resolution in real-world applications

A) Spatial Resolution

Spatial resolution was measured by imaging a point source (0.3 mm in diameter Na-22 source encased within an acrylic cube with dimensions of 10 mm ×10 mm ×10 mm) across the FOV. The original activity of the Na-22 source was 111 kBq (3 µCi) and the calibrated activity of the source during these experiments was determined to be 89.9 kBq.
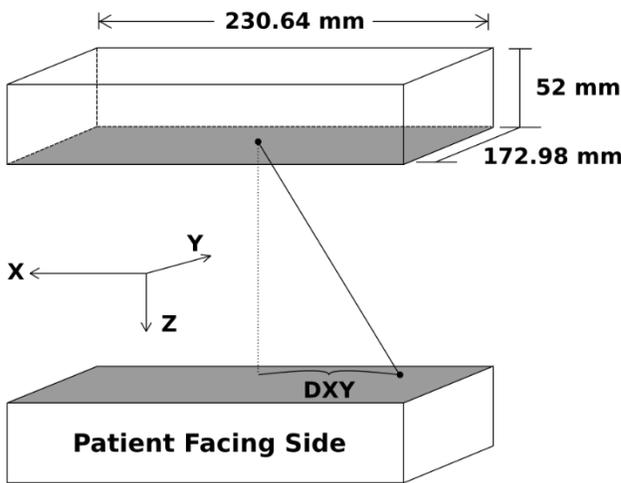
Fig. 15: Schematic showing the overall size of the detector heads, and the axis convention.

Profiles of each source were created in ImageJ[35] by plotting through the maximum intensity pixel of the source and measuring the image gray value along that line. An image pixel size of 0.2 mm for the XY plane and a voxel depth of 2.67 mm was used for the image matrix size throughout the spatial resolution analysis.

49

Two reconstruction methods were implemented for the analysis of spatial resolution, both the standard MLEM reconstruction and a back-projection reconstruction. Spatial resolution was reported in terms of full width at half-maximum (FWHM) and full width at tenth maximum (FWTM) of the point spread function (PSF) which were determined from a gaussian fit of the data distribution. Here we followed a widely adopted practice for PSF characterization[36–38] although this slightly deviated from NEMA NU-4 requirements that derives FWHM from line profiles drawn through the image of the point source. It is also noted that no background activity was included with the point source acquisitions.

The separation between the detector heads was kept at 80 mm for each point source acquisition. First, spatial resolution was evaluated at the center of the XY FOV half the distance between the detector heads (i.e., at x=0 and y=0). Then the resolution was measured as a function of the distance from the center of the XY FOV along the X and Y axes at a Z location of one quarter the detector head separation. Each measurement was calibrated to run until more than 100,000 prompt counts were acquired. Resolution was quoted for each axial direction as either X, Y, or Z resolution corresponding to the direction of the profile across the image.

Additionally, the micro-hotspot phantom was used for the qualitative assessment of system resolution through the visualization of its small rods. The phantom was filled with 1 MBq of ^{18}F-FDG and acquired for 40-minutes with a detector head separation of 89 mm, that was dictated by the phantom size. The phantom was immobilized by the detector heads and placed centrally in the X and Y directions. For image reconstruction, a pixel size of 0.2 mm × 0.2 mm was used to allow for visualization of smaller details. Post processing of the micro-hotspot phantom was

50

implemented in ImageJ with a 3D gaussian blur (sigma = 1.0) and with an unsharp mask (sigma = 7.0, mask weight = 0.6).

B) Sensitivity

The same Na-22 point source from the spatial resolution analysis was used for evaluating sensitivity. The source was placed in the center of the XY plane halfway between the detector heads and moved along the X-axis with a step of 2 mm using a stepper motor stage spanning the full FOV resulting in 113 slices for which sensitivity has been calculated. At each step an image of a Na-22 point source was acquired; the acquisition was calibrated to acquire list mode data for 60 seconds, yielding enough events for the analysis. Detector heads were separated by 60 mm during each acquisition. Each data set was reconstructed with an SSRB image processing algorithm. Values of the per-slice sensitivity S_i (18) and the absolute per-slice slice sensitivity $S_{A,i}$ (19)[33] were determined and plotted as a function of source location in the FOV.

$$S_i = \left(\frac{R_i - R_{B,i}}{A_{Cal}}\right) \tag{18}$$

$$S_{A,i} = \left(\frac{S_i}{0.9060}\right) \times 100 \tag{19}$$

where R_i is the count rate measured for slice i, $R_{B,i}$ is the background count rate for slice i, and A_{Cal} is the calibrated activity of the source. Absolute sensitivity was calculated with the branching ratio of Na-22 (ie: 0.9060) and the calculated sensitivity S_i for slice i. The normalized system sensitivity was determined by summing the per-slice sensitivity across the FOV and dividing by the number of datapoints.

C) Count rate performance

A NEMA NU4 (rat) scatter phantom was used for the determination of count rate statistics. The phantom consists of a long cylindrical high-density polyethylene (0.98 g/cm^3) with a diameter of 50 mm and a length of 150 mm. A cylindrical cavity with a diameter of 3.5 mm drilled lengthwise through the phantom at an axial offset of 17.5 mm was filled with 51 MBq of F-18 to make the line source. The line source was closed at each end with a 4 mm long syringe port, as a result of which the line source length was 142 mm.

The phantom was placed at the center of the XY FOV (y=0) parallel to the X axis halfway between the detector heads with a separation of 60 mm. Multiple acquisitions were started as soon as the phantom was filled and were programmed to perform an acquisition every 15 minutes to acquire a maximum of 29 million events in total. The measurements were run from the initially high activity for 20 hours, until the phantom had decayed through 10 half-life's and was left with little to no activity in the last acquisitions.

Data processing for count rates involved reconstructing list mode acquisition data files using LOR acceptance angle filtration (i,e., only LORs whose endpoints that have certain ΔX and ΔY referred to as "Angle Allowance" were used for image processing). The resulting files were then processed using an SSRB image reconstruction technique. Peak count rates were determined from the plots of count rates vs phantom activity concentration.

NECR performance was evaluated over a clinically relevant activity range and efficiency at peak noise equivalent count rate was determined as the peak NECR normalized to the activity at the peak (20):

52

$$Eff_{NECR,\ peak} = \left(\frac{NECR_{Peak}}{A_{Peak}}\right) \qquad (20)$$

D) <u>Clinical Imaging</u>

The Radialis PET camera was tested; it is currently in use for a clinical trial[39] at the Princess Margaret Cancer Centre of the University Health Network (UNH-PMCC) in Toronto, Canada. Participants in the study received a clinical indication for diagnostic medical imaging tests like full-field digital mammography (FFDM) with or without digital breast tomosynthesis (DBT), or breast MRI, or WB PET/CT scan.

Women with a newly diagnosed breast cancer were injected with ^{18}F-FDG in the range of activities between 37 and 307 MBq (activity is chosen randomly and does not depend on the clinical case). Each participant rests for 60 minutes to allow for the ^{18}F-FDG uptake. Some participants receiving WB PET/CT were first imaged with the Siemens Biograph Vision WB PET/CT scanner (image acquisition time ~30min) and immediately after that they were taken for another imaging session with the Radialis system (single image acquisition time ~5 min at each position). Obtaining WB-PET/CT and Radialis PET images permits direct comparison between the two PET imaging modes. For some patients that WB PET/CT was not indicated, they were imaged with Radialis PET system and the breast imaging modalities (i.e., FFDM, FFDM-DBT, MRI) alone or in combination. Optionally, patients who received 185 MBq of ^{18}F-FDG returned in two hours so that ^{18}F decays to ½ of the initial activity, and then imaged with the Radialis system for a second time (i.e., low-dose organ-targeted imaging session).

2.4   Results

A) <u>Spatial Resolution</u>

Results of the average spatial resolution as a function of point source location along the Y-axis and X-axis are presented in Table 3, and in Fig. 16 showing the X, Y, and Z MLEM resolutions as functions of location. The values of the PSF full width at tenth maximum (FWTM) are also provided in addition to the spatial resolution values in terms of FWHM. In-plane spatial resolution, determined by the X and Y resolution plots, has an average value of 2.3 ± 0.1mm. The resolution for the system along the Y direction stays consistent across the entire FOV with an average value of (2.3 ± 0.1) mm. Similarly, the resolution along the X direction of the system maintains a FWHM of (2.2 ± 0.1) mm. As expected, the cross-plane or Z resolution of the system is about three times larger than in-plane resolution and has an average value of (6.8 ± 0.7) mm within the central FOV.

Results from the same acquisition reconstructed with a back projection (BP) algorithm without filtering are presented in Fig. *17*. As expected, application of a BP degraded the resolution along all axes. The in-plane resolution for the central Z axis location is on average 3.3 ± 0.1 mm and the cross-plane resolution is 16.4 ± 0.1 mm.

The reconstructed image of the micro-hotspot phantom presented in Fig. 18 demonstrates the visualization of small sources down to the 1.35 mm diameter rods while using the MLEM reconstruction and down to the 1.7 mm diameter rods with the back-projection reconstruction. As expected, MLEM reconstructed images exhibited less noise and better image contrast. This agrees with the calculated spatial resolution since it is conventionally accepted that the FWHM point

54

source spatial resolution is 1.4-2 times the size of the smallest resolvable pattern in nuclear imaging devices[40].
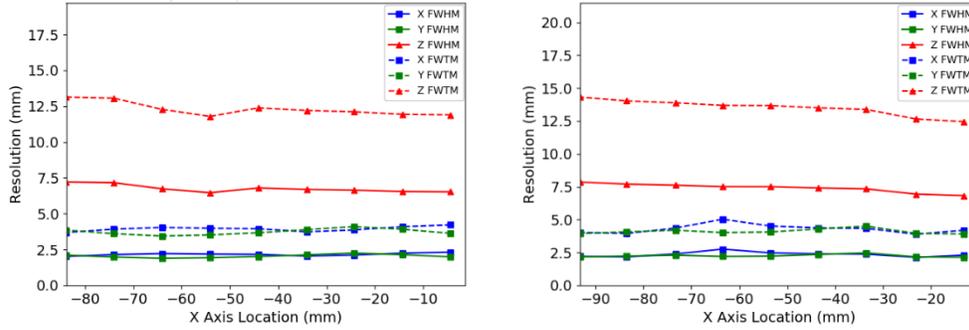
Fig. 16: System spatial resolutions produced with the MLEM reconstruction. Left: The central Z Axis resolution plotted as a function of point source location along the X Axis. Right: Quarter Z Axis resolution plotted as a function of point source location along the X Axis.
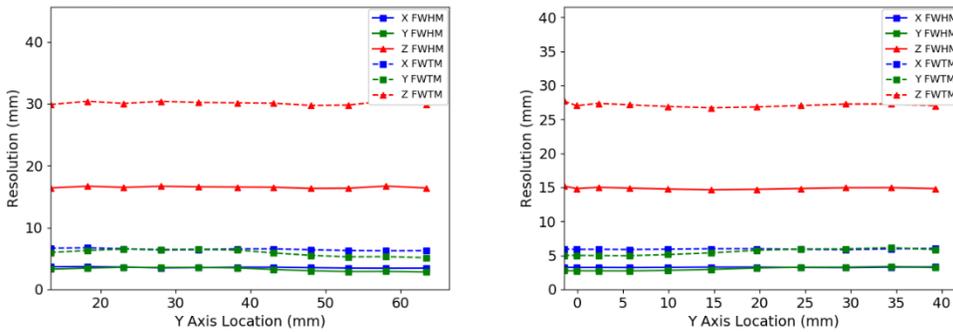
Fig. 17: System spatial resolutions produced with a BP reconstruction. Left: The central Z Axis resolution plotted as a function of point source location along the X axis. Right: Quarter of the Z Axis resolution plotted as a function of point source location along the X axis.
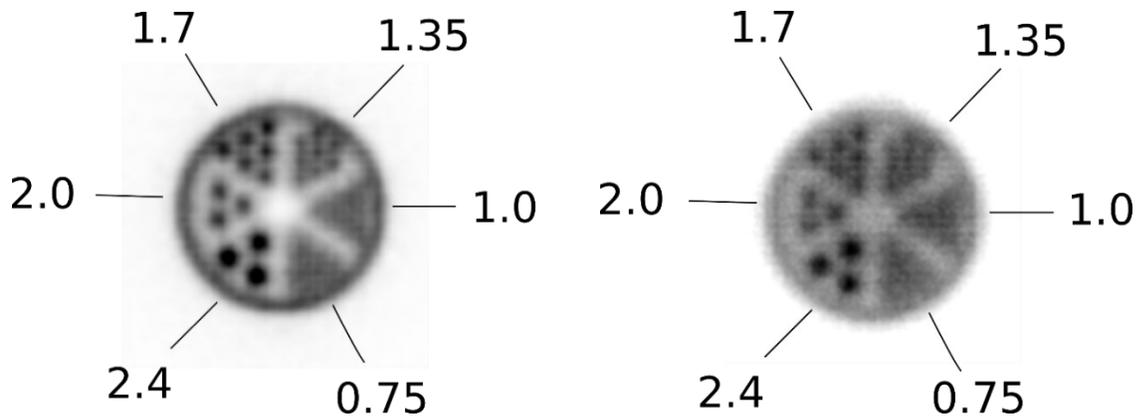
Fig. 18: Images of the micro-hotspot phantom reconstructed using an MLEM reconstruction (Left) and with a BP reconstruction (Right).

Summary of MLEM System Spatial Resolutions

Table 3: Average values of spatial resolution in terms of the X, Y, and Z FWHM and FWTM for a detector head separation of 80mm

	At Z=0			
	X axis		Y axis	
Resolution	FWHM	FWTM	FWHM	FWTM
In-plane X (mm)	2.2±0.1	4.1±0.2	2.4±0.2	4.4±0.4
In-plane Y (mm)	2.2±0.1	4.1±0.2	2.3±0.1	4.1±0.1
Cross-plane Z (mm)	7.8±0.3	14.2±0.5	6.6±0.9	12.1±1.7
	At Z=20 mm			
	X axis		Y axis	
Resolution	FWHM	FWTM	FWHM	FWTM
In-plane X (mm)	2.4±0.2	4.3±0.3	2.5±0.1	4.5±0.1
In-plane Y (mm)	2.2±0.1	4.1±0.2	2.2±0.2	4.1±0.3
Cross-plane Z (mm)	7.3±0.5	13.3±0.9	6.9±0.6	12.7±1.0

B) Sensitivity

Sensitivity values for the system are displayed as functions of point source location along the X-axis in Fig. 19 and are summarized in Table 4. A peak per-slice sensitivity value of 32 cps/kBq is shown at the center of the FOV that after normalizing to the branching ratio of Na-22 gives peak absolute per-slice sensitivity of 3.5%. Fig. 19 demonstrates the details of the measured NEMA sensitivity profile along X-axis slices: as expected, sensitivity gradually decreases when the source is moved towards the edge of the detector head since the LOR's solid angle decreases. Total normalized system sensitivity is determined as the sum of each single value along the plot, divided by the number of data points, and is equal to 2.4%.
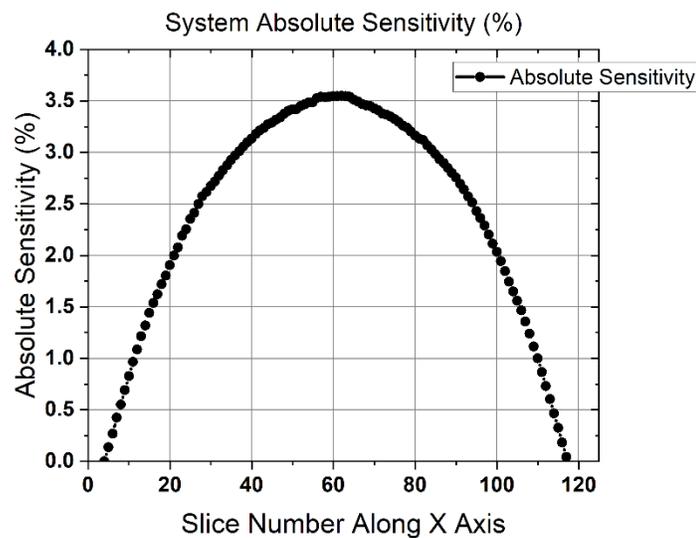
Fig. 19: Per-slice Absolute Sensitivity plotted against point source location along the X axis.

Summary of Sensitivity values

Table 4: The peak per-slice absolute sensitivity and the normalized total sensitivity for a 60 mm detector head separation

Detector Separation	60 mm
Peak Absolute Slice Sensitivity	3.5 %
Peak Slice Sensitivity	32 cps/kBq
Normalized Total Absolute Sensitivity	2.4%

C) <u>Count rate performance</u>

Count rates for the system are plotted against the scatter phantom activity concentration and include the prompt, true, scatter, noise equivalent, and random count rates in Fig. 20. Activity concentrations corresponding to specific standard uptake values (SUV) are marked on each count rate plot (SUVs are calculated for different clinically relevant injected activities for a 77.3 kg woman). The values of SUV = 1 are included to estimate the activity that would be expected for the background tissue during acquisition. Peak count rates are summarized in Table 5 for several different LOR angle allowance filters. As this is evident from Fig. 20, peak Noise Equivalent Count Rates (NECRs) were achieved at a phantom activity concentration of 10.5 kBq/mL with an efficiency at peak NECR of 5,650 cps/MBq. The scatter fraction for the 90 mm and 110 mm LOR angular filters are 24% and 31% respectively. Use of a 52 mm LOR angle allowance filter further reduces the scatter fraction to 6.2% accompanied by a cut to the overall count rates.
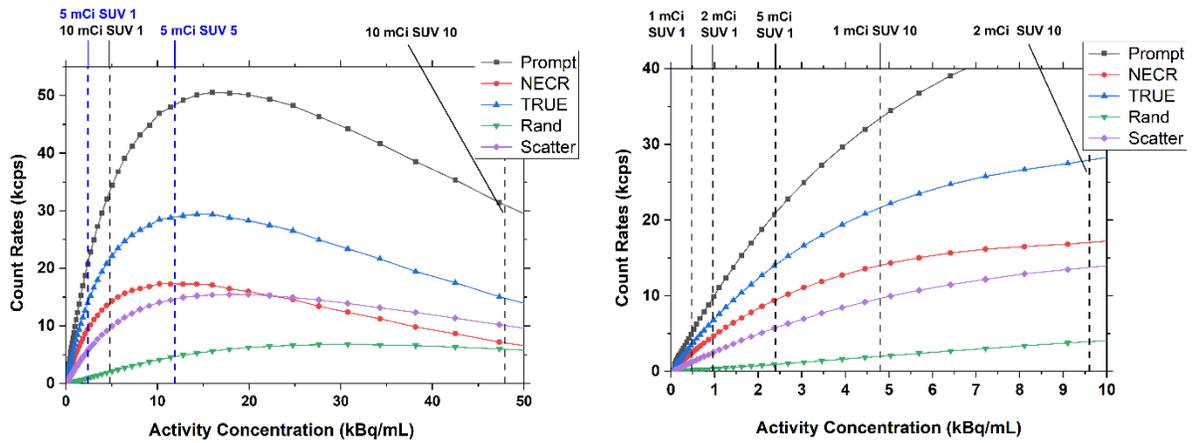
Fig. 20: System performance count rates for a 90 mm LOR angle allowance

Summary of Count Rates based on the LOR angle filter applied

Table 5: Summarized values for count rates at different LOR angle allowance parameters.

	52 mm Angle Allowance (kcps)	90 mm Angle Allowance (kcps)	110 mm Angle Allowance (kcps)	144 mm Angle Allowance (kcps)
Peak NECR	9.6	17.3	17.8	18.1
Peak True Rate	13.8	28.5	32.5	36.4
Peak Prompt Rate	19.7	46.9	59.3	73.1
Peak Scatter Rate	4.15	13.9	20.9	29.3
Peak Random Rate	1.63	4.35	5.76	7.31

D) Clinical Imaging

Fig. *21* compares the FFDM craniocaudal (CC) view (Fig. 21, A) with one selected low-dose Radialis PET slice in a CC view (Fig. 21, B) acquired in a 56-year-old female with histopathology diagnosed invasive ductal carcinoma and intermediate-grade ductal carcinoma in situ (DCIS). For the PET imaging, the patient received intravascular 37 MBq of ^{18}F-FDG, and the scanning

59

performed 1 hour after that injection. The focal uptakes on Radialis PET image (arrow and arrowhead in the Fig. 21, B) corresponded to one mass (arrow Fig. 21, A) detected on FFDM, however the other mass that was also histopathology proven was detected only in Radialis PET images despite using a low dose of ^{18}F-FDG. The second cancer was not detected by mammography even in retrospect because of the dense breast tissue masking effect.
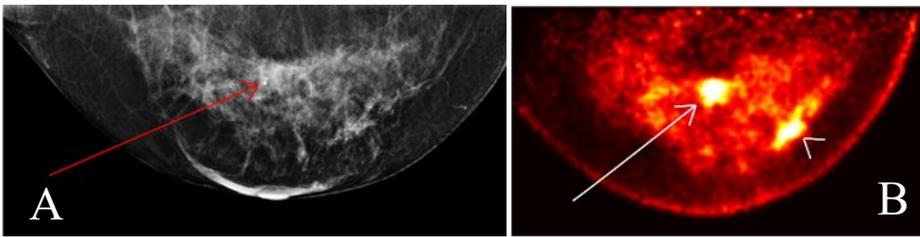
Fig. 21: A 56-year-old female with invasive ductal carcinoma and intermediate-grade DCIS. Digital mammography of right breast (A) and right breast Radialis PET image with 37 MBq ^{18}F-FDG injection (B) both in the same projection (CC view) are presented for comparison between these two imaging modalities. Cancers are demonstrated by the arrows (A, B) and arrowhead (B). The second cancer (arrowhead) is visualized only by Radialis PET (B).

Fig. 22 shows the comparison among multimodality images, specifically digital breast tomosynthesis (DBT) synthesized mammography CC view (Fig. 22 A), MRI axial subtracted view (Fig. 22 B), and two Radialis PET camera CC view images (Fig. 22 C, D) obtained from a 61-years old woman with a known malignant disease involving the lateral aspect of the right breast. For the organ-targeted PET acquisition, 178 MBq of ^{18}F-FDG was administrated and two subsequent imaging sessions at 1 hour (Fig. 22 C) and 4 hours (Fig. 22 D) post injection were acquired. The PET images showed that changes in image contrast with time as activity decreases were not impactful for the radiologist visual assessment of multifocal cancers. Both Radialis PET images demonstrate ^{18}F-FDG uptake in the extensive malignancy that corresponds to the irregular mass detected on synthesized mammography and to a single irregular shape mass demonstrated by MRI images. However, the Radialis PET images are more reproducible of histopathology

findings with multiple foci of cancers. Even after 4 hours, the PET image (Fig. 22, D) still shows that the cancer is not a single mass, but it is indeed a group of multiple distinct masses spanning an area of contiguous contrast enhancement on MRI or distortion on DBT images.
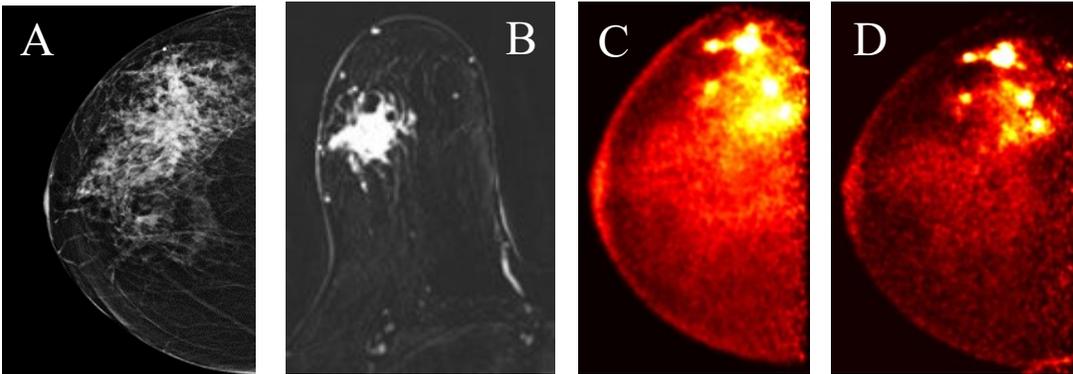
Fig. 22: A 61-year-old female with right breast multifocal invasive and in situ ductal carcinoma. Images of the same breasts: A) a selected slice of digital breast tomosynthesis (DBT) in the CC plane showing extensive distortion; B) a selected slice of MRI in the axial plane showing one irregular shape enhancing mass lesion after 2 min post gadolinium-chelates based contrast administration; C) 3D Radialis PET in the CC plane where multiple distinct regions of contrast uptake after 1 hour of 178 MBq ^{18}F-FDG injection; (D) 3D Radialis PET in the CC plane where the conspicuity of the multiple regions of enhanced ^{18}F-FDG uptake (indicative of multifocal cancers) remains after 3 hours from the prior (C) acquisition.

Fig. 23 shows the results of FFDM and Radialis PET Camera imaging in a 50-year-old female with a palpable breast lump against the chest wall. The mediolateral oblique (MLO) digital mammography image identified a single palpable mass. Radialis PET camera images were acquired with 200 MBq of injected activity, revealing two additional masses along the patient's chest wall, which surgical pathology confirmed as malignancy.
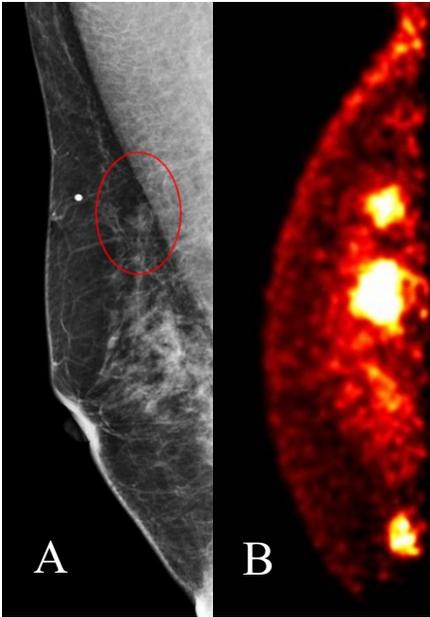
Fig. 23: The MLO view digital mammography image (A) demonstrated the palpable mass (red circle) associated with the radiopaque marker placed on the patient's skin. The presented slice of Radialis PET camera CC image with 200 MBq injected ^{18}F-FDG (B) identifies this lesion against the chest wall as well as two additional posterior masses. The 3 total masses identified by Radialis PET were biopsy confirmed cancers.

Fig. 24 presents an illustration of the problems dealing with MRI recalls for likely benign lesions or false positive MRI results. The MRI 3D maximum intensity projections images (Fig. 24 A) show multiple rounded and oval shape enhancing masses in both breasts. There is a noticeable discrepancy of MRI depicted lesions with the lack of focal uptake of ^{18}F-FDG in the Radialis PET images acquired with a 37 MBq injection. This patient underwent programmed bilateral breast surgery (mastectomy) without malignancy identified in surgical pathology report.

The clinical WB PET images presented in Fig. 25 were acquired with a Siemens Biograph Vision WB PET/CT. Fig. 25 (A) shows the full FOV slice with the region of the image with the breast expanded in Fig. 25 (B) and the

Radialis PET Camera Fig. 25 (C) of a 50-year-old patient with a known malignancy in the right breast. 307 MBq of ^{18}F-FDG was administered and the WB PET/CT image acquisition was performed after a 60-min uptake time. Immediately after the WB PET/CT examination the patient was imaged with the Radialis PET Camera. The WB PET/CT axial images identified an inhomogeneous hypermetabolic mass and a slightly hypermetabolic satellite nodule. Despite the shorter imaging time for the Radialis PET acquisition (5 min) the extent of the lesions is more clearly defined, both in terms of the extent of the lesions as well as the regions within the lesion

with the highest functional activity. Smaller anatomical features such as the nipple are visible in the organ-targeted image while not being present in the WB images.
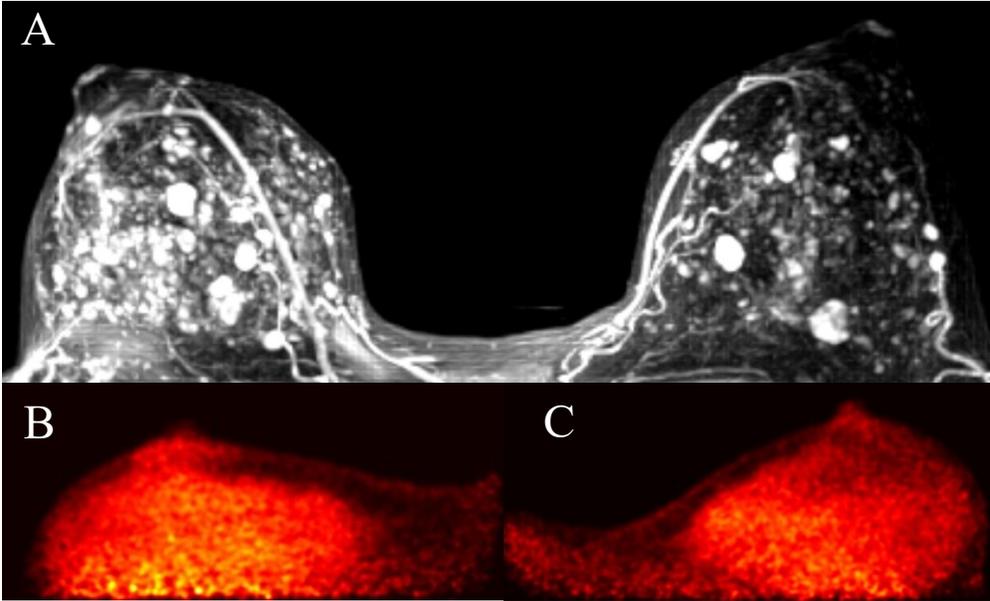
Fig. 24: A 33-year-old high-risk female underwent pre-operative breast MRI with multiplicity of enhancing masses demonstrated by the 3D-MIP image (A) and without corresponding masses demonstrated by the Radialis PET camera images (B) with a 43 MBq injection. The mediolateral oblique views from the Radialis PET camera are presented for the left (B) and right (C) side without evident focal ¹⁸F-FDG uptake in either image. The surgical pathology results do not show signs of cancer.
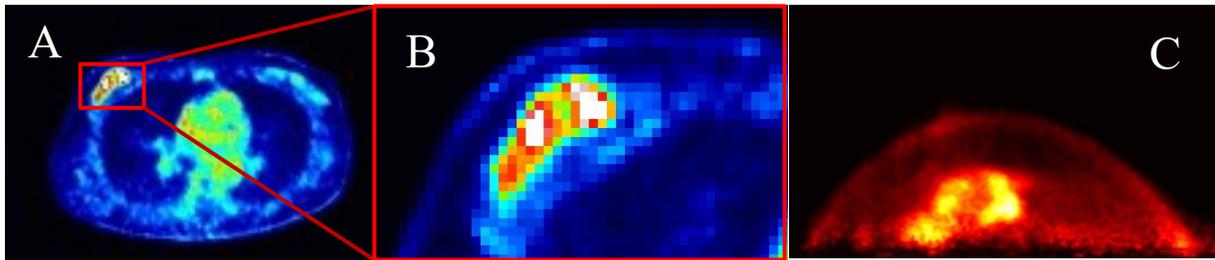
Fig. 25: Side by side comparison of 307 MBq PET images from a breast cancer patient scanned with a Siemens Biograph PET/CT reconstructed using a time-of-flight reconstruction technique (TOF) (A and B) and with the Radialis PET system (C).

2.5 Discussion

Despite the proven value of using radiotracers in a broad spectrum of diagnostic procedures in oncology, cardiology and neurology, the effective radiation dose limits the use of PET imaging in undiagnosed patients as well as repeat studies. It also limits the numerous opportunities for using PET in screening, especially for breast cancer, which is increasingly justified due to well-known limitations of X-ray mammography and breast MRI[41–43]. Overall, to realize the full potential of molecular imaging with PET, including organ-targeted devices, PET count sensitivity should be significantly improved. For breast examinations the effective radiation dose should not exceed that of X-ray screening procedures with digital mammography or DBT. Also, enhanced sensitivity will allow for reduced scanning time, thus improving patient throughput and the utilization of PET devices.

The development of the organ-targeted Radialis PET technology described herein focused on improving the sensitivity and NECR performance over a clinically useful activity range including low-dose activities. This approach was taken so that the count rate at low doses can ensure sufficient statistical quality in the PET images. At the same this will allow for a short acquisition time under the administration of standard doses.

The developed technology can be used in different clinical applications since it allows to attain the highest possible angular coverage of different organs including the breast, prostate, and the chest (for cardiac imaging). The first clinical evaluation of the developed organ-targeted PET camera was devoted to breast cancer. The rational for this choice is the clinical significance of high-sensitivity molecular breast imaging with ^{18}F-FDG PET: it has the potential to overcome a well-

64

known drawback of mammography that is low sensitivity in heterogeneous and extremely dense breasts[44] found in roughly 50% of the population[45]. Since breast ^{18}F-FDG PET uptake is largely independent of breast tissue density, it is capable of overcoming the lesion obscurity in mammography from dense breast tissue. We also demonstrate a potential to address the high false-positive rate associated with gadolinium-enhanced breast MRI. These advantages for breast cancer detection are demonstrated with clinical images.

Several PET systems have been developed for imaging clinically relevant breast cancers with performance independent of breast density and hormonal changes[16,44,46]. Breast-targeted PET systems differ from WB PET detectors in both geometry (using either planar or ring detectors) and positioning of the breast during image acquisitions. The Naviscan Positron Emission Mammography (PEM) Flex Solo II, uses two planar compression heads positioned on either side of a breast, containing line detectors that scan across the FOV. The reported in-plane spatial resolution for the Flex Solo II PEM using MLEM reconstruction is 2.4 ± 0.2 mm[37] – a significant improvement over WB PET (that is 5-7 mm[47,48]), and cross-plane resolution is 8.2 ± 1.0 mm[15]. However, since moving detectors collect less of the injected radiation signal at any given time, this method results in longer acquisition times, decreased peak slice sensitivity and peak slice absolute sensitivity (0.2% & 1.8 cps/kBq) and higher effective dose exposures (370 MBq injection[49]). Despite this fact the Naviscan system has a higher sensitivity than MRI for the smallest cancers (in part since it is not angiogenesis-dependent)[50,51,52].

A more recent organ-targeted PET technology is Mammi Breast PET developed by Oncovision. It uses a circular array of 12 detectors (or two circular arrays in high sensitivity configuration). The patient lies prone and the breast hangs pendulant into the ring. Although the ring design allows for

65

greater sensitivity and faster scanning times it has reduced imaging capabilities for lesions near the chest wall[13]. The peak per-slice absolute sensitivity of this system is improved compared to the Flex Solo II system, with 1.8% for the single ring configuration, and is further improved to 3.1% with the dual ring configuration due to slightly thicker crystals (12 mm thick versus 10 mm scintillation crystals in the single ring system) and a larger detection area[53,54]. The ring configuration of the MAMMI PET system is able to achieve nominally higher point source resolution[54] than the Radialis PET Camera (1.5-1.9 mm vs. 2.2-2.4 mm), however the sensitivity for identifying clinically relevant cancers also depends on the overall efficiency of activity detection. In this aspect, peak-slice sensitivity and peak-absolute-slice sensitivity of the Radialis PET camera is larger than in both the Flex Solo II and Mammi Breast PET systems.

Another parameter that characterizes the efficiency of activity detection in PET imaging is NECR which describes the true coincidence rate that would give the observed signal to noise ratio (SNR), or the same level of statistical noise, if there were no randoms and no scattered events. This value encapsulates the sensitivity of each device for its entire FOV during scans with an appropriate concentration of activity and contains a composition of effects based upon both the detector sensitivity as well as the geometric efficiency related to the design of the scanner. Moreover, this method of describing sensitivity enables a comparison between WB PET and organ-targeted PET as the NEMA calculations for Peak NECR, Concentration at Peak NECR and Activity at Peak NECR, is analogous in both types of systems (thus the efficiency at peak count rate is a fair comparison). Measurements are performed with volume sources within the FOV to compare the translation of overall activity into imaging events. In contrast, the NEMA-NU2 method for measuring system sensitivity for WB PET systems with a line source is fundamentally different

66

than the NEMA-NU4 method, which is often adapted for organ-targeted systems, that uses a point source which makes a significant difference in the nuances of the values of sensitivity.

Table 6 presents the efficiency at peak count rate for several PET systems including organ-targeted, whole-body and total-body systems. It can be seen that the Radialis PET camera exhibits much higher efficiency at peak count rate when compared to current WB systems. The SiPM-based total body PET technology of uExplorer[55] also provides superior sensitivity in comparison to the WB systems, achieved with detectors that completely cover the axial length of a patient's body. Radialis' SiPM-based organ-targeted technology uses the same approach: the coverage of the Radialis system is larger than the organ being imaged and improves the sensitivity from the increased axial extent of the detectors.

Optimized for low-dose imaging, the count rate for the Radialis PET Camera peaks at relatively low activity values. However, Fig. 20 illustrates that the coincidence count rate capabilities and the dead time that the system experiences for standard clinical doses is still high. The equivalent SUV values are indicated for a standard clinical range of injected activity from 185 to 370 MBq (5 to 10 mCi) as well as low-dose 37 MBq (1 mCi) imaging. For SUV 1-7 at 370 MBq the count rates are no worse than 78% of the peak NECR.

67

Table 6: Values for efficiency at peak count rate are calculated from the peak NECR data reported for each system

PET System	Efficiency at Peak Count Rate (cps/MBq)	Peak NECR (kcps)	Concentration at Peak NECR (kBq/mL)	Phantom Volume (mL)	Activity at Peak NECR (MBq)
Radialis PET Camera (NU-4)	5,650	17.8	10.5	300	3.15
uExplorer[55] (NU-2) (Total Body)	3,790	1440	16.8	22,600	380
Oncovision Mammi PEM Dual Ring (NU-4)[54] (PEM)	1,260	34.0	31.2	866	27.0
GE Discovery IQ[47] (PET/CT)	618	123.6	9.1	22,000	200
GE Discovery MI (NU-2)[56] (PET/CT)	581	266	20.8	22,000	458
Phillips Vereos (NU-2)[57] (PET/CT)	556	646	52.8	22,000	1,160
GE Signa PET[11] (PET/MR)	524	218	17.8	22,600	402
Siemens Biograph Vision (NU-2)[58] (PET/CT)	435	306	32	22,000	704
Naviscan PEM Flex Solo II (NU-4)[15] (PEM)	393	10.6	90	300	27.0

In clinical settings, the higher sensitivity and the fact that the count rate peaks at relatively low activity values, are translated into a possibility to reduce the activity of the injected radiopharmaceutical.

Typically, protocols for breast imaging with a dedicated PET system requires an injection of 370MBq (10 mCi) of ^{18}F-FDG[16,39], resulting in an effective dose to the breast of 3.4 mGy and an effective whole-body dose of up to 6.2–7.1 mSv[25,49]. This effective dose is more than 10 times the average effective dose of 0.5 mSv for digital mammography[25,49] and poses a significant risk of radiation-induced cancer from annual PET scans. For the radiation-induced cancer risks from nuclear medicine techniques to be appropriate for screening women with dense breasts, the injected ^{18}F-FDG activities need to be reduced to 70 MBq or less[49]. This represents an effective radiation dose of ~1.3 mSv, which is estimated to be equivalent to the effective dose from combined FFDM with DBT[25].

Fig. 21 illustrates the capability of the Radialis PET Camera to image with 37 MBq of activity (10 times lower than the standard dose), suggesting further study of the clinical sensitivity for breast cancer detection with 70 MBq of radiotracer is warranted.

Images taken after two different time intervals (Fig. 22) demonstrate the image quality at a reduced count rate due to radiotracer decay as well as increased lesion-to-background ratio over time due to the different wash out mechanism for cancerous and background tissue[59]. With the camera's high sensitivity for low count rate acquisitions, the images present a stronger discrimination of multiple foci over time even though the activity is reduced through the decay of the injected radioactivity.

69

Fig. *23* demonstrates the importance of thin detector heads of the Radialis PET Camera and the small distance to the front of the field of view for improving the visualization of deep chest lesions – a recognized challenge for breast-specific PET systems[60,61]. This is an important differentiation from pendulant breast PET systems where it has been found that lesions that were outside the field of view due to being located close to the chest wall "could not be imaged even with special attention to patient positioning"[1].

2.6 Conclusion

Along with the scintillator material and photosensor characteristics, the main element that influences PET sensitivity is scanner geometry, which includes the active area of the PET detector intercepting annihilation events[62,63]. Here we show that the sensitivity of organ-targeted PET can be significantly improved with planar detector geometry provided that the FOV and the distance between two detectors are appropriate for the solid angle available for the collection of annihilation radiation. The optimization of the planar FOV was achieved through the use of tiled block detectors combined with high-yield scintillation crystals, high-gain solid-state photodetectors, temperature control, and acquisition electronics architected for the application. Clinical demonstration with imaging in breast revealed that the Radialis PET technology is well-suited to identifying cancers even at a 10-fold dose reduction in comparison with standard WB PET dose. At a standard dose of ^{18}F-FDG, images acquired with Radialis PET camera show clinical detail that cannot be seen with commercial WB PET scanners.

The demonstrated capability for imaging with 37 MBq suggests that Radialis organ-targeted PET technology could be used in low-dose clinical applications such as breast and prostate cancer

70

screening, the multiple examinations required for prostate cancer patients on active surveillance, and cardio-vascular examinations. High quality organ-targeted imaging may also be particularly well-suited to applications with emerging targeted radiotracers.

3   Section 3 –Image Quality Evaluation for the Clinical Prototype High-Sensitivity Organ-Targeted Radialis PET Camera

The following section contains the content from the manuscript: J. Stiles, O. Bubon, H. Poladyan, B. Baldassi, A. Reznik, "Image Quality Evaluation for the Clinical Prototype High-Sensitivity Organ-Targeted Radialis PET Camera" with the intent to be published to the Journal of Nuclear Medicine.

Image Quality Evaluation for the Clinical Prototype High-Sensitivity Organ-Targeted Radialis PET Camera

Justin Stiles[1*], Oleksandr Bubon[1,2], Harutyun Poladyan[3], Brandon Baldassi[1], Alla Reznik[1]

1 - Lakehead University, Thunder Bay, Canada

2 – Radialis Medical, Thunder Bay, Canada

3 – Thunder Bay Regional Health Research Institute, Thunder Bay, Canada

*email: jtstiles@lakeheadu.ca

3.1   Abstract

The newly developed clinical prototype of an organ-targeted Positron Emission Tomography (PET) camera from Radialis Medical is tested with a set of tests proposed for standardized testing of Positron Emission Mammography (PEM) systems. Imaging characteristics related to standardized uptake value (SUV) and detectability of small lesions, namely spatial resolution and linearity, uniformity, and recovery coefficients, were measured.

In-plane spatial resolution is measured as 2.3 mm ± 0.04 mm, spatial linearity is 0.1 mm, and flood field and phantom uniformity is 11.7% and 8.3% respectively. Recovery coefficients at different lesion to background ratios for the system demonstrate a contrast of between 18-35% of the true activity for a 4 mm sphere and a contrast of between 65-70% of the true activity for an 8 mm sphere. Sources 6 mm in diameter or larger can be confidently detected based on the Rose criterion and should have an accurate contrast assignment for the SUV measurement at different lesion to background ratios. Phantom reconstructions for the NEMA small animal phantom demonstrate a recovery coefficient of 0.21 for the 1 mm rod and up to 0.89 for the 5 mm rod. Combined with the high sensitivity demonstrated previously with the standardized NEMA NU-4-2008 tests and

example patient images acquired at 1/10 of the standard activity of 2-[fluorine-18]-fluoro-2-deoxy-D-glucose (^{18}F-FDG), this should allow early cancer detection at low-doses suitable for screening.

3.2 Introduction

The development of a high-sensitivity organ-targeted Positron Emission Tomography (PET) system – the "Radialis PET camera" – has spurred from the clinical need to reduce the radiation dose associated with functional (molecular) imaging while preserving the detectability of small lesions inherent to organ-targeted PET[12,24,37,64]. We have recently demonstrated that the Radialis PET camera has improved sensitivity, capable of significant dose reduction (factor of 10) in comparison to commercial whole-body (WB) PET scanners[65]. Standardized evaluation measurements were performed with NEMA NU-4 procedures adapted for the planar PET detector geometry; test included spatial resolution, sensitivity, and system count rates. Selected clinical breast cancer images were also presented to illustrate the system performance within a range of circumstances including varied radiation doses (37-370 MBq), presence of chest wall lesions, and lesion detectability in comparison to WB-PET, full field digital mammography (FFDM), and MRI. Increased sensitivity shown by NEMA NU-4 tests and high-efficiency radiotracer detection demonstrated with clinical images were made possible by the development of a new type of modular detector architecture with four-side tileable sensor modules based on high-gain Silicon Photomultipliers (Si-PMs) photosensors[28].

Standardized measurements with NEMA NU-4[65] are important to compare the Radialis PET camera to similar modalities, but these standards were developed over 10 years ago and so they do not include a consideration of the latest hardware and software developments within the field and

74

therefore have faced recent criticism[34]. Indeed, the requirements of using backprojection image reconstruction do not represent the reconstruction methods used in real-world applications, and the described tests themselves have potential flaws when it comes to accurately representing the system performance metrics[34]. In addition, since NEMA NU-4 standard tests were developed for preclinical imaging, they do not take into account the specifics of clinical organ-targeted PET (e.g., relatively large field-of-view (FOV)) and different detector architectures including planar PET detector heads and modular design used in the Radialis PET camera[65].

Therefore, a comprehensive assessment of image quality in organ-targeted PET requires additional tests that characterize imaging parameters not covered by NEMA NU-4 standard and which are more suitable for the intermediate FOV and modern iterative image reconstruction methods. We follow the methodology developed by others[37,66] to perform tests of: spatial resolution and linearity, flood field uniformity, and recovery coefficients (RC) with micro-spheres. Evaluation with NEMA NU-4 image quality phantom is also included for comparison with the results of these method. The tests of RC with micro-spheres in a hot background and flood field uniformity, which are not included in NEMA NU-4, paired with contrast to noise ratio (CNR) and the Rose Criterion are of importance for assessing the ability of the system to apply standardized uptake value (SUV) analysis to lesions of different size and uptake of a radiopharmaceutical. Additionally, the modular design of our system inherently involves variability in the electronic functions between separate modules. These differences may cause spatial distortions along the FOV, thus requiring experiments with line sources (rather than point sources used in NEMA NU-4) and large-area flood phantoms which can properly identify any discrepancies in spatial resolution, image signal to noise ratio and uniformity within the entire image space.

75

3.3   Materials and Methods

Radialis PET camera utilizes a planar detector configuration that makes it versatile for imaging different organs including the breast, prostate, and heart, with the first application of the technology in breast imaging. For the breast-targeted system, 12 sensor modules are arranged in a 3×4 array to make a planar detector head (Fig. 26). For image acquisitions two detector heads are positioned on either side of the immobilized breast. The size of an individual module is 58×58 mm^2, which results in a sensor area of 174×232 mm^2 and provides a sufficient field-of-view to fully cover an entire breast. Additionally, the detector heads are enclosed in a thin housing material allowing for the active imaging area to be ~4 mm from the edge of the detector housing. The detailed information of the Radialis PET technology can be found in the previous publication: "Evaluation of a High-Sensitivity Organ-Targeted PET Camera"[65].

Fig. 26: Configuration of the Radialis PET Camera with two planar detector heads to be positioned on either side of a breast

An iterative maximum likelihood expectation maximization (MLEM) algorithm is used for image reconstruction. This reconstruction is ideal for the planar detector geometry as opposed to using a limited angle tomographic reconstruction. The MLEM algorithm implements a variable number of iterations – with 15 iterations currently being used for clinical reconstructions. Additionally, a median root prior (MRP) filter[32] is applied within the reconstruction to introduce image blurring.

76

Reconstructed images are saved as DICOM images with a stack of 24 images of the XY plane. The image matrix is defined by a pixel size of 0.4 mm × 0.4 mm. The image slices have a thickness determined by the detector separation divided into 24 slices and is varied between each acquisition.

.
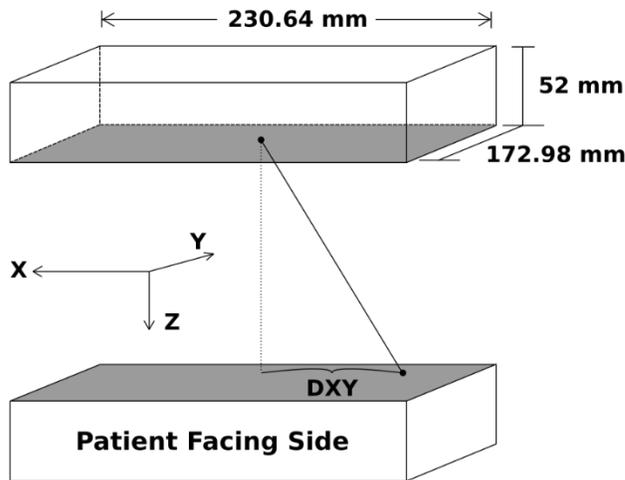
Fig. 27: Detector Schematic showing the overall size of the detector heads, and the axis convention.

A) Spatial Resolution & Linearity

The method for determining spatial resolution is adapted from the NEMA NU-2 standards for WB PET cameras and involves analyzing the point-spread function of a line source[12,58,67].

To make a line source, a capillary tube, with a length of 44.4 cm and an inner diameter of 1.2 mm, was filled with F-18 solution; it was placed half-way between the detectors and positioned centrally in the y-axis such that the entire x-axis FOV was covered by the source. Coincidences were collected until at least 1 million events were recorded for image reconstruction. The reconstructed image was analyzed by taking the point spread function (PSF) orthogonal to the axis of the tube. The full width on half a maximum (FWHM) of a gaussian fit for the PSF defines the spatial resolution being quoted here[68]. PSFs were taken across the source in 10 locations across the FOV. The average value of the FWHMs was reported as the spatial resolution for the in-plane and cross-plane FOVs.

Spatial linearity was measured with a linearity phantom shown in Fig. 28. Six capillary tubes were filled with ^{18}F-FDG solution and positioned into parallel trenches engraved into a sheet of plastic such that the distance between the tubes is 20 mm.
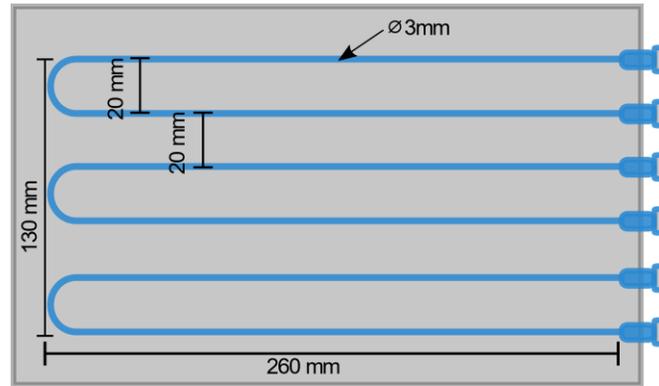
Fig. 28: Schematic diagram of the spatial linearity phantom with markings for the line source separation and total phantom size.

The phantom was imaged two times in two different positions in the FOV as follows:

In the central XY plane (z = 0 mm), with capillaries parallel to y-axis.

In the central XY plane (z = 0 mm), with capillaries parallel to x-axis.

Measurements of spatial linearity were derived from plots of the image gray value perpendicular to the length of the capillary tubes. The location of the peak pixel values of each of the six capillaries was determined and the separation between each of these peaks was plotted.

B) Flood Field Uniformity

A flat phantom that is large enough to cover the whole field of view was used[69]. The phantom was a 100 uCi ^{18}F-FDG flat source positioned parallel to the detectors between the detector head – at the same distance from each detector head. Separation between the detectors is set to 80 mm. At least 5 million coincidence events were acquired with energy window set to 350-750 keV.

78

The acquired data was used to perform per-pixel efficiency corrections and conduct the uniformity analysis. After per-pixel efficiency correction and geometric efficiency correction, the image of the flat phantom was reconstructed with the clinical reconstruction software (MLEM MRP beta = 0.5) using images from the first iteration and fifteenth iteration. In the resulting images a 150 mm × 100 mm ROI was chosen to extract the statistical measurements.

Measurements of the mean pixel value, percent standard deviation, maximum, and minimum grey value were all tabulated. These values were calculated based on the methods described for determining the uniformity of the NEMA NU-4 small animal phantom[33] and are further explained in the Phantom Images section below.

C) Recovery Coefficients

Recovery coefficient phantoms consisted of two 500 mL IV bags with a set of micro-spheres placed between them. The acquisition layout is presented in Fig. 29. The spheres, with inner diameters of 4, 5, 6, and 8 mm, were each filled with the same activity concentration. The IV bags were also filled with activity and the activity concentrations of the bags were recorded. The ratio between the activity concentration of the spheres and the background was 4:1, 10:1, and 17:1 with background concentrations of 5 kBq/mL, 0.379 kBq/mL, and 0.286 kBq/mL and sphere activity concentrations of 20 kBq/mL, 3.79 kBq/mL, and 5 kBq/mL respectively. A reconstruction of each acquisition was performed with the default MLEM reconstruction with 15 iterations and a median root prior filter applied (beta=0.3).
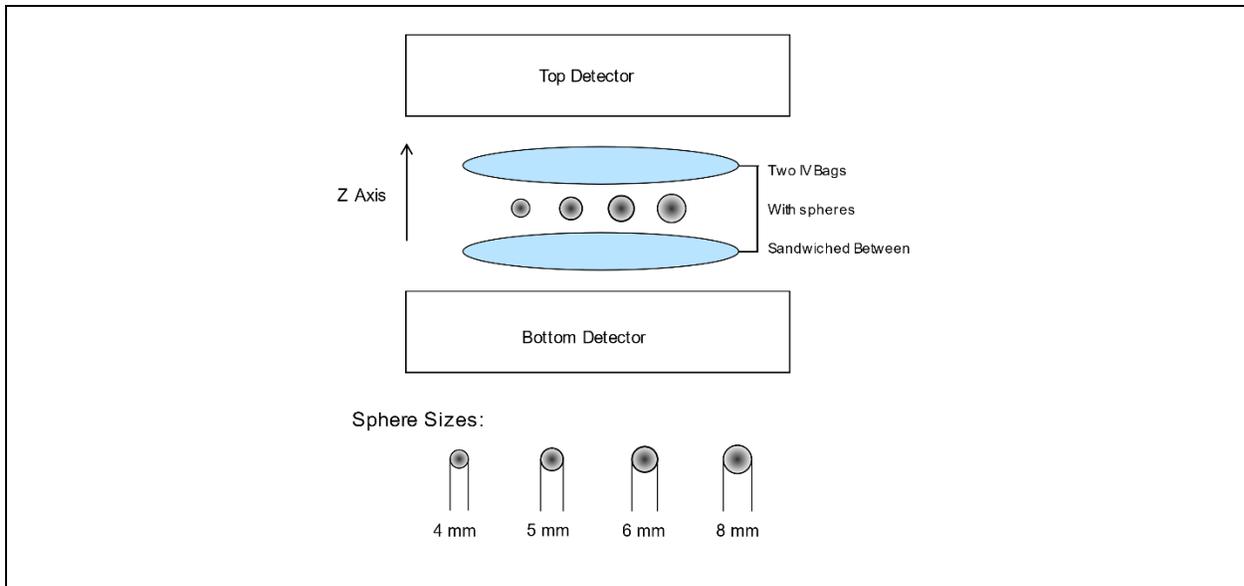
Fig. 29: Acquisition layout for the recovery coefficient experiment with the micro sphere set placed between two IV bags. Micro sphere sizes are presented below the diagram.

The recovery coefficients determined were the maximum relative recovery coefficients based on the calculations according to NEMA standards[67] and is shown in (21). The mean contrast of the uniform part of the IV bag was taken as the mean for the background within the recovery coefficient calculation. A region of interest around each sphere was used to take the maximum image gray value of each sphere. This maximum value was taken as the representative measured activity for the sphere in question. These values were recorded for each sphere in the image and plots of the recovery coefficient as a function of sphere size were created.

$$RC_{max} = \frac{maximum\ (Sphere\ ROI)}{mean\ (background)} \tag{21}$$

Values for both recovery coefficient and relative recovery coefficient were determined from the measured image values, with the relative recovery coefficient representing the explicit source to background ratio and the standard recovery coefficient being normalized to the measured activity ratio between the sphere and background activity concentrations.

The contrast to noise ratio was calculated based on the absolute difference between the mean counts in the hot spheres and the background (for the slice with the maximum hot sphere counts) and was normalized to the standard deviation of the background (22). This value was used to determine the detectability for each source based on the Rose Criterion which states that a CNR < 5 fails and is considered not detectable. Based on this, pass or fail values for each sphere in the three lesion to background ratio (LBR) acquisitions was reported.

	$$CNR = \frac{|C_H - C_B|}{SD_B}$$	(22)

D) <u>Image Quality Phantom</u>

NEMA NU 4 image quality phantom (Fig. 30) contains hot lesions in the form of hot rods, as well as uniform, hot, and cold regions. The hot rods have different diameters and positions in the cold solid background. The measurement of recovery coefficients in the hot rods is used for the assessment of spatial resolution and partial volume effects of the scanner, whereas the noise and uniformity measurement in the uniform region gives insight into the signal to noise ratio and the performance of the attenuation and scatter corrections, respectively.

The total activity of 1.87 MBq in the phantom was determined from the calibrated activity concentration and the fillable volume of the phantom. The two cold chambers of the phantom were filled with water and air to provide cold spots in the uniform hot region of the phantom. The acquisition was calibrated to acquire at least 10 million total events for accurate image reconstruction and processing.

The image of the phantom was reconstructed with the same correction and reconstruction parameters as is used for clinical imaging. The analysis was performed to measure image uniformity, recovery coefficients and accuracy of data corrections. The procedure of the analysis is outlined below.
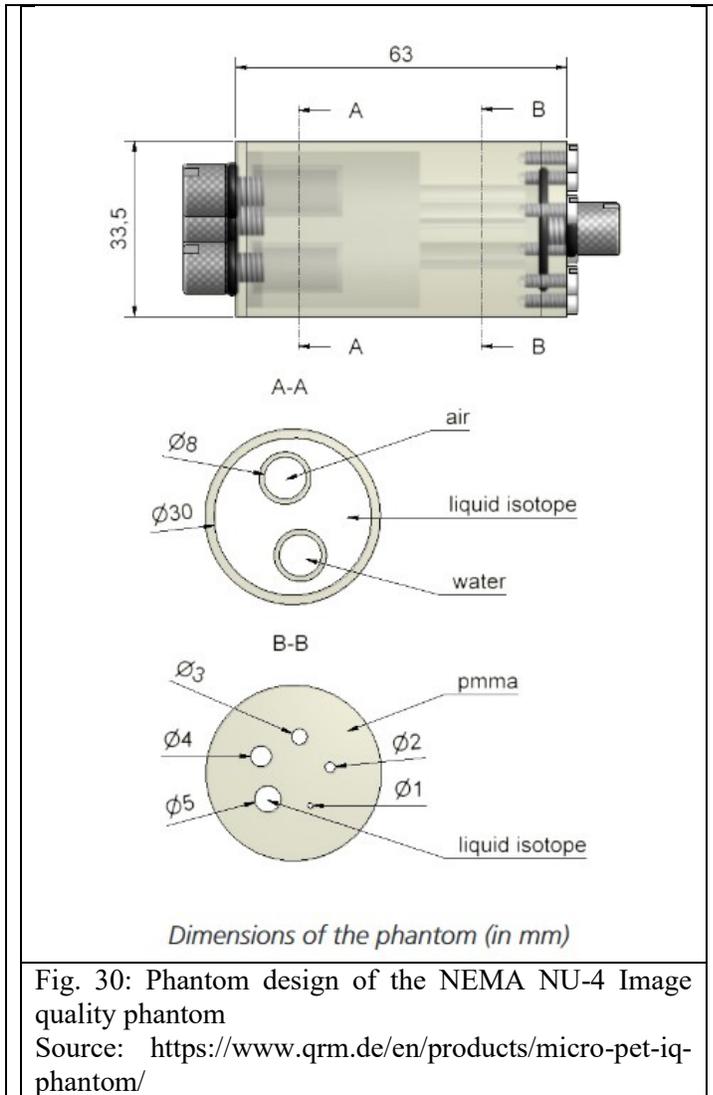
For the measurement of the uniformity a cylindrical volume of interest (VOI) with diameter of 22.5 mm and height of 10 mm was selected in the central uniform region of the phantom. The average activity concentration, the maximum and minimum voxel values in VOI, and the percentage standard deviation (%STD) was measured and reported.

For the measurement of the recovery coefficient the voxel values of the central 10 mm of the hot rods were averaged to obtain a single image slice with lower noise. Around each hot rod a circular region of interest (ROI) was drawn with diameters twice the physical diameter of the rods. The pixel position with the maximum value in each ROI was identified.

Fig. 30: Phantom design of the NEMA NU-4 Image quality phantom
Source: https://www.qrm.de/en/products/micro-pet-iq-phantom/

The transverse line profile through the identified maximum pixel was drawn along the rods. The mean pixel values measured for each profile was divided by the mean activity concentration measured in the uniformity calculation to determine the recovery coefficient for each hot rod.

The standard deviation of the recovery coefficients is calculated as follows:

$$\%STD_{RC} = 100 \times \sqrt{\left(\frac{STD_{lineprofile}}{Mean_{lineprofile}}\right)^2 + \left(\frac{STD_{background}}{Mean_{background}}\right)^2} \tag{23}$$

For the measurement of the accuracy of the corrections a cylindrical volume of interest (VOI) with diameter of 4 mm and height of 7.5 mm was selected in the central region of the cold chambers. The ratio of the mean in each cold chamber to the mean of the hot uniform area was reported as spill-over ratio (SOR).

The standard deviation of the SOR is calculated as follows:

$$\%STD_{SOR} = 100 \times \sqrt{\left(\frac{STD_{cold}}{Mean_{cold}}\right)^2 + \left(\frac{STD_{background}}{Mean_{background}}\right)^2} \tag{24}$$

3.4   Results

A) <u>Spatial Resolution & Linearity</u>

Resulting images from the spatial resolution acquisition are shown in Fig. 31. The averaged spatial resolution across the in-plane FOV is 2.3 ± 0.04 mm and similarly the averaged Z-axis resolution is 7.9 ± 0.7 mm.
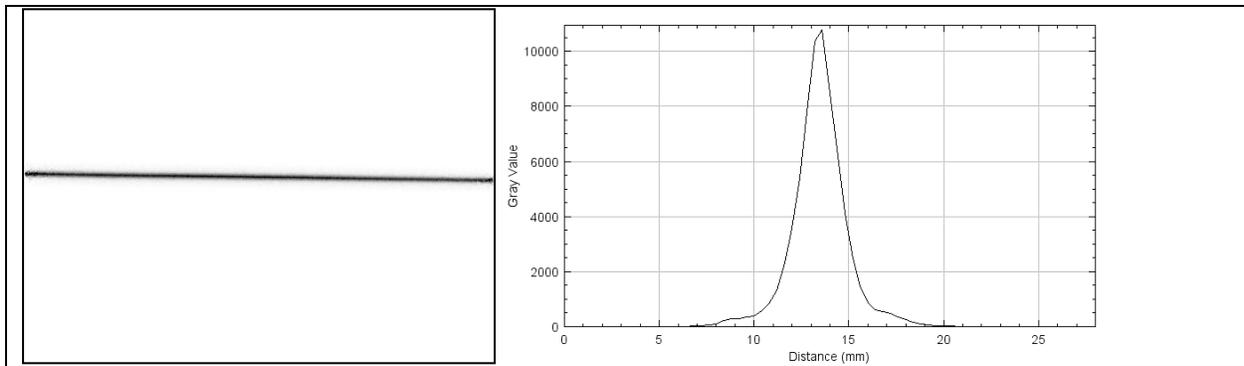
Fig. 31: Image of the capillary phantom centered along the Y axis with a corresponding profile taken along the Y axis.

Spatial linearity for both the X and Y axes are derived from the plots of the reconstructed position of each source. The spatial accuracy of each reconstructed source is plotted in Fig. 32 & Fig. 33 as the position error as a function of source location. Reconstructed source positions have an inaccuracy of 0.1 mm along both axes.
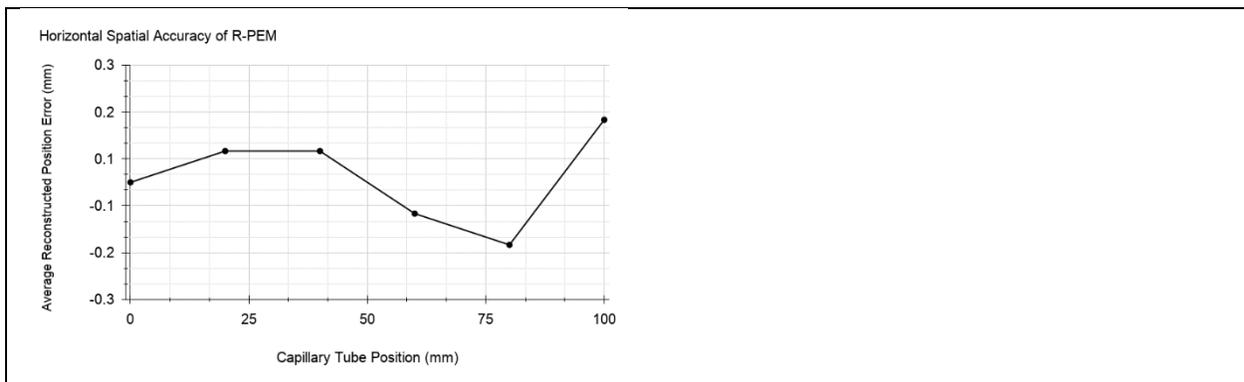
Fig. 32: Plot of the difference between the reconstructed source locations compared to the expected location of the linearity phantom positioned along the X axis.

84
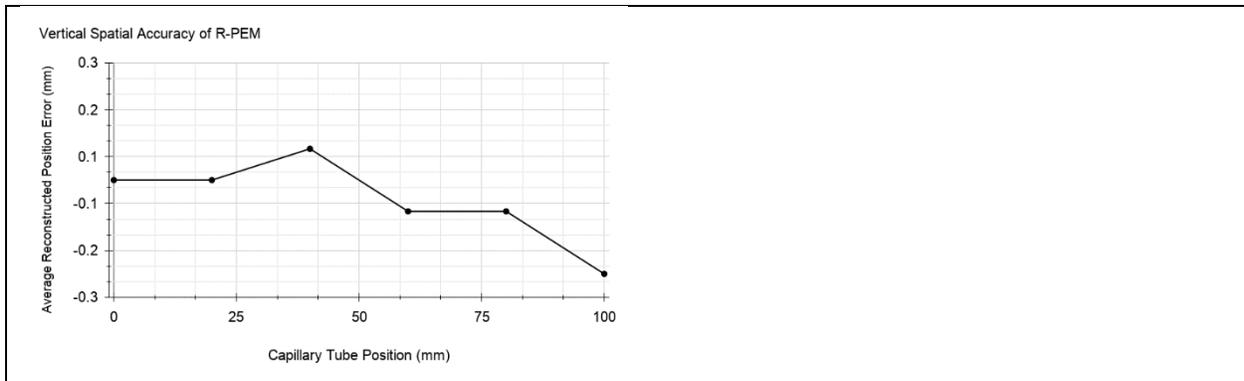
Fig. 33: Plot of the difference between the reconstructed source locations compared to the expected location of the linearity phantom positioned along the Y axis.

B) Flood Field Uniformity

Images of flood sources are displayed in Fig. 34 (Left) for the 1st MLEM iteration and in Fig. 34 (Right) for the 15th MLEM iteration. Reported values for uniformity are summarized in Table 7.
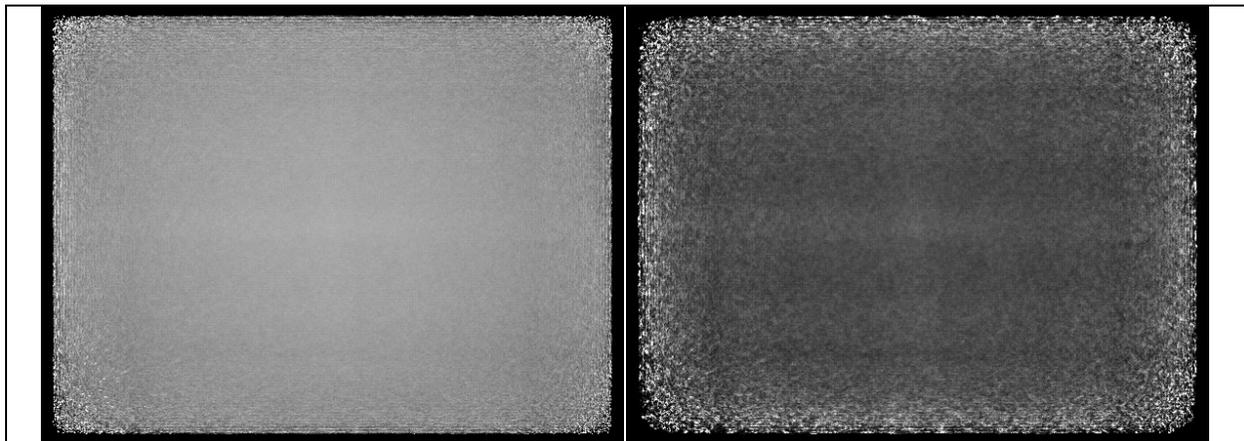
Fig. 34: Image of the uniform phantom reconstructed with 1 iteration (Left) and 15 iterations (Right).

Table 7: Results of Uniformity for the 1st and 15th iteration reconstruction of both.

Iterations	Mean	% STDEV	Min	Max
1	1515	4.1	1228	1717
15	1014	11.7	580	1769

C) Recovery Coefficients

85

Reconstructed images for the acquisitions of a 4:1, 10:1, and 17:1 lesion to background activity concentration ratio are displayed in Fig. 35 with the corresponding point-spread function across the hot spheres. Calculations of the recovery coefficients for each sphere in each activity distribution are derived from the measured peak values in each lesion.

Fig. 35: Images of the IV bags with the hot spheres placed in-between with the corresponding profiles across the spheres. The lesion to background activity concentration ratio is as follows: 4:1 (left), 10:1 (center), and 17:1 (right).
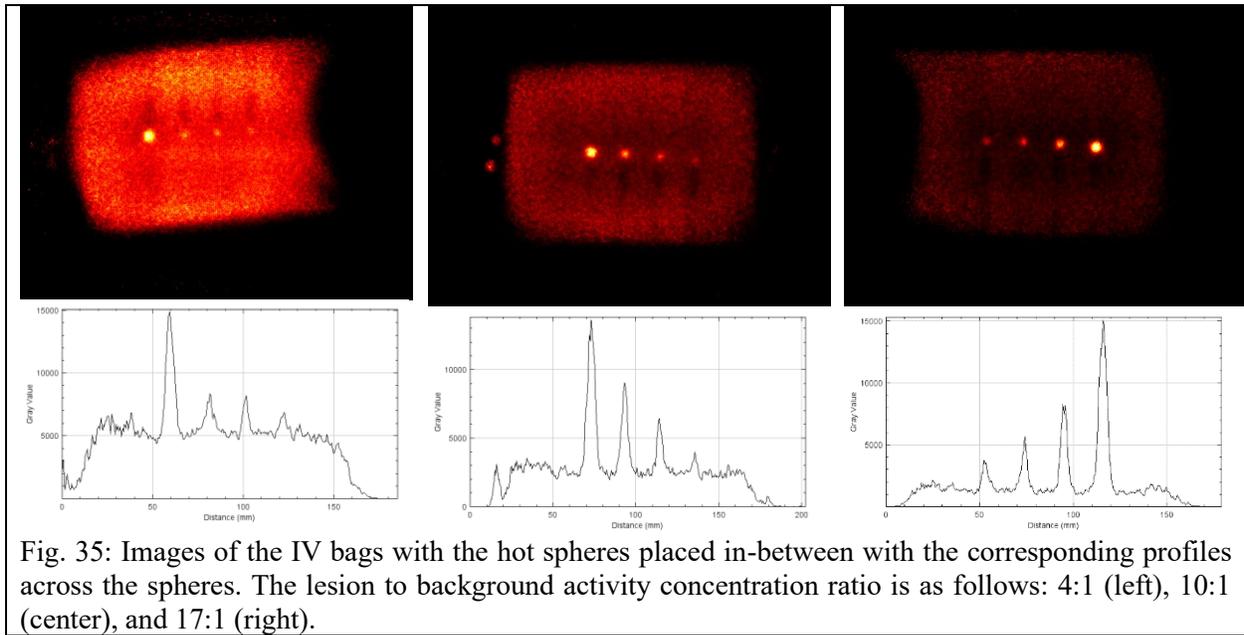
Recovery coefficients are summarized in Table 8 for the three lesion to background ratios of the 4 sphere sizes.

Table 8: Summarized recovery coefficients for the associated lesion to background ratios.

Sphere Size	4:1 RC	10:1 RC	17:1 RC	4:1 Relative RC	10:1 Relative RC	17:1 Relative RC
4 mm	0.354	0.185	0.191	1.42	1.85	3.24
5 mm	0.400	0.281	0.282	1.60	2.81	4.79
6 mm	0.425	0.419	0.461	1.70	4.19	7.84
8 mm	0.700	0.650	0.666	2.80	6.50	11.31

Table 9 contains a summary of the contrast to noise ratio for each of the RC acquisitions as well as the corresponding pass or fail determined from the Rose Criterion.

86

Table 9: Contrast to Noise ratio for each LBR for the four spheres with the corresponding pass or fail indicator for the rose criterion.

CNR	17:1	Rose Criterion	10:1	Rose Criterion	4:1	Rose Criterion
8 mm	61.4	PASS	22.7	PASS	12.8	PASS
6 mm	19.2	PASS	11.2	PASS	5.7	PASS
5 mm	9.3	PASS	5.1	PASS	2.8	FAIL
4 mm	5.9	PASS	2.2	FAIL	0.42	FAIL

D) Image Quality Phantom

Images of the selected slices from the NEMA NU-4 Image Quality Phantom in Fig. 36 shows the regions of the hot rods, uniform region, and empty reservoirs.
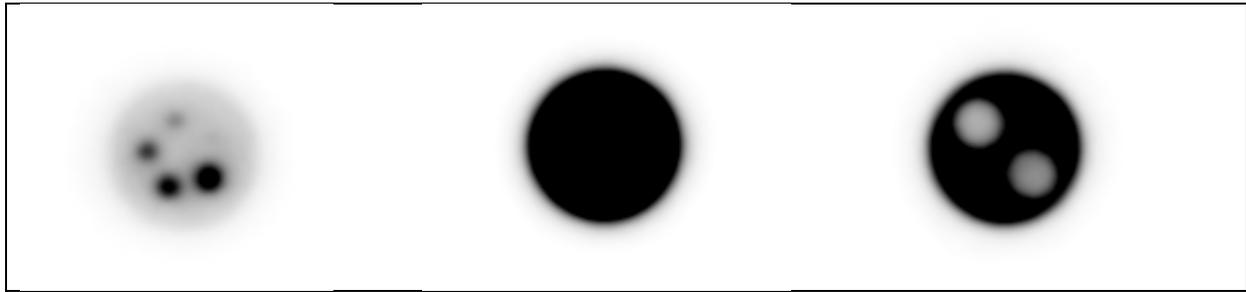
Fig. 36: Reconstructed image slices for the NEMA NU-4 image quality phantom displaying the hot rods for recovery coefficients (Left), Uniform region (center), and the air and water reservoirs (Right)

Uniformity measurements are presented in Table 10. The uniformity for the phantom is an 8.31% standard deviation from the mean grey value of 12,322 within the uniform region.

Recovery coefficients derived from the phantom, presented in Table 11, show a trend towards full contrast recovery for increasing source sizes. For the smallest 1 mm source a recovery coefficient of 21% with an uncertainty of 16% was measured.

Spill-over ratio for the water and air-filled reservoirs are tabulated in Table 12. The air-filled cylinder has a SOR of 0.20 while the water-filled cylinder has a SOR of 0.30.

87

Table 10: Uniformity derived from the image of the NEMA NU-4 image quality phantom uniform region.

	Mean	Maximum	Minimum	%STD
Uniformity	12322	14707	10499	8.31

Table 11: Recovery coefficients and the percent standard deviation for the 5 hot rods in the NEMA NU-4 phantom.

Rod Diameter	Recovery coefficient	%STD
1 mm	0.21	16.0
2 mm	0.31	9.4
3 mm	0.53	9.9
4 mm	0.73	8.8
5 mm	0.89	8.8

Table 12: Measured spill-over ratio and percent standard deviation for the NEMA NU-4 phantom.

Region	SOR	%STD
Water-filled cylinder	0.30	18.98%
Air-filled cylinder	0.20	29.18%

3.5   Discussion

The image quality necessary for proper clinical implementation of an organ-targeted PET camera is dependent on the accurate reconstruction of radiation distributions. Differences in the signal gain between detector modules can cause variations in the results of spatial resolution, linearity, and uniformity across the FOV. Another more fundamental limitation has to do with the system's non-zero spatial resolution and partial volume effects, which lead to a reduced contrast assignment and blurred edges around objects. Because of the uncertainty in contrast assignment, small sources of radiation tend to smear out across the image, with a proportional reduction in observed contrast or activity. This affects the contrast recovery coefficients of the PET camera and reduces the ability to accurately assess SUV in small lesions in reconstructed images; the exact severity of this effect is discussed with the results presented here. Since the only system with a planar detector head

design and comparable experimental tests is the Flex Solo II PEM, discussed comparisons with organ targeted PET are only made with that system.

A) Spatial Resolution & Linearity

Spatial resolution measured with the line source was 2.3 ± 0.04 mm for the in-plane and 7.9 ± 0.7 mm for the cross-plane resolution is consistent with previous point source measurements[65].

The reconstructed linearity phantoms from this system demonstrate an accurate congruence across the entire FOV. Source peaks from the linearity phantom are reconstructed to within 0.1 mm of the expected locations in images across both the X and Y axes and shows a high degree of congruence between the expected and measured source locations. This result shows no deviation from the straight-line sources, which correlates to no image distortion across the FOV.

B) Image Uniformity

The image of the flood field phantom has a uniformity across the FOV of 11.7% standard deviation from the mean value for the 15th iteration. For the 1st iteration the standard deviation from mean is 4.1%, an expected improvement due to the nature of iterative maximum likelihood reconstruction algorithms[70]; indeed, it is well known that the expectation-maximization algorithm becomes noisier and has large distortions near edges with increased iterations. Compared to flood field uniformity, the small animal phantom has a measured standard deviation of 8.3% for the 15th iteration. It is evident in the results of small animal phantom uniformity, which shows similar results between Radialis PET, pre-clinical scanners, and PEM[15,71], that this system produces a comparable uniformity response when the area in question is reduced. Increased non-uniformity for the larger ROI can be mitigated with further uniformity corrections or image blurring.

89

The flood field experiment is adopted to compare to the test for PEM scanners and deviates from NEMA in the size of the region of interest that is being analyzed. For the NEMA phantom analysis image uniformity is determined for a small volume of interest located in the central slices of the phantom, and for the uniformity test defined for PEM six smaller ROIs drawn on the in-plane image slices of the flood field phantom are used. The size of the ROI which we used for the determination of flood field uniformity (150×100 mm^2) is much more representative of the FOV of the Radialis camera and is more accurate for characterizing the response from the entire FOV, including wide ranging distortions.

It is useful for organ targeted PET cameras to measure both the flood field uniformity and small animal phantom uniformity. The ability of a scanner to register a small uniform activity concentration as flat is as important as the full field effects of uniformity since the fluctuations within small regions of interest can affect the observed properties of smaller lesions. Because of this, both distributions should be considered when testing an organ targeted PET camera for image uniformity.

C) <u>Recovery Coefficients</u>

The setup of this experiment involves the use of a lesion activity concentration which is 4×, 10×, and 17× the background concentrations. This is different than the activity distribution of recovery coefficients that the NEMA phantom requires, which uses the same activity concentration for the phantom's hot rods and the uniform background and doesn't require the background activity to be within the same slice as the sources being measured. Since the radiation distribution of this measurement closely mimics the type of radiation distributions seen in clinical practice, the results

of this analysis are extremely valuable as an analogue to clinical imaging. These results suggest that lesions that are 6 mm in size are visible in any circumstance and, depending on the uptake ratio of a malignancy, lesions as small as 4 mm are detectable based on rose's criterion.

For the NEMA phantom the smallest 1 mm phantom rod has a 21% contrast recovery with a standard deviation of 16%. The largest rod in comparison has a contrast recovery of 89%. Each of the 4 largest rods have approximately the same standard deviation between 8-9%. The measured contrast recovery of the phantom is comparable to pre-clinical systems[72–74], which are understood to have very high spatial resolutions and exceptional detectability for small lesions in small animal studies. A contrast recovery which is similar to these pre-clinical devices suggests the Radialis organ targeted PET camera is well-suited for implementation in clinical imaging for smaller early-stage cancers.

Compared to reported values for PEM[37] the results for the 4:1 and 10:1 recovery coefficients are a significant improvement; where PEM reaches a relative recovery coefficient of 2 at a sphere diameter of 15 mm, the Radialis PET camera has a relative recovery coefficient of 2 for a sphere diameter of between 6-8 mm. When compared to the highest-performing whole body PET, which has values on the order of 30% recovery for an 8 mm sphere[66], the Radialis PET camera shows an improvement with a recovery of 70% for an 8 mm sphere. This is attributed to the improvements to spatial resolution for the Radialis PET camera.

Contrast to noise ratio for the micro spheres results are increased compared to WB PET[66]. The cutoff for detectable size based on the Rose Criterion for WB PET was ~8 mm for the 4:1 concentration ratio, and ~6 mm for the 8:1 concentration ratio. Our results show an improvement

91

to those values with the smallest detected spheres being 6 mm for a 4:1 ratio and 5 mm for a 10:1 ratio. No other breast targeted devices characterized the CNR, or the detectability based on Rose's criterion, and as such only a comparison to WB PET is considered.

Measured recovery for the 6 mm sphere stays consistent regardless of the LBR, while the two smaller spheres seem to exhibit larger variation in contrast recovery for changing LBR. While the activity of 6 mm sources is still underestimated by approximately 50-60%, consistent recovery can be used to monitor treatment response for sources larger or equal to this size. During treatment as the functional activity of the source decreases the same amount of underestimation will occur. Conversely, contrast recovery of the smaller sources has a stronger dependence on LBR and would seem to artificially increase in activity as the LBR drops, resulting in positive treatment response appearing less effective than it is.

The determination of spatial resolution may inform of the intrinsic detectability of this system in a laboratory setting; however, the clinical circumstances of the utilization of this device are often much more complex than a simple line source. Our experiments confirm that spatial resolution doesn't reveal the actual ability of a system to correctly identify small sources, due to partial volume effects. Based on the rose criterion, sources greater than 5 mm can be confidently detected in clinically analogous circumstances. Compared to an in-plane spatial resolution of 2.3 mm, RC results quantify the lower limits of detectability as it relates to clinical source distributions which involve lesions in an active background.

The goal of increasing system spatial resolution for PET has always been a sought-after achievement for improving clinical performance of these devices. However, this investigation

shows less dependence on spatial resolution for the limits of the detectability of small lesions in clinical conditions. There is a relationship between the two, obviously, where partial volume effects caused by non-zero spatial resolution causes the decrease in apparent lesion activity, and thus a decrease in SUV and detectability. This may suggest, however, that there is less diagnostic value to increasing spatial resolution by fractions of a millimeter, but instead perhaps utilization of partial volume corrections (PVC) can translate into more significant clinical improvements. There is currently no agreement within the community on what approach to take for PVC or its clinical usefulness[75–78] but given that the lower limits of detectability for clinical PET seem to be approaching a plateau based on improved resolution, PVC may find increasing value for today's organ targeted PET devices which focus on small lesion detection.

3.6   Conclusion

Given there are no standardized experimental analyses for determining the image quality of an organ-targeted PET camera, apart from the brief investigation outlined in NEMA NU-4, a hybridized evaluation based on NEMA NU-4, NEMA NU-2, and some of the recommendations for PEM systems are considered. In-plane spatial resolution is measured to be 2.3 mm ± 0.04 mm and spatial linearity is accurate to within 0.1 mm. Image flood field uniformity is 11.7% and small animal phantom uniformity is 8.3%. Recovery coefficients for the system result in a contrast of between 18-35% of the true activity for a 4 mm sphere and a contrast of between 65-70% of the activity for an 8 mm sphere for three different source-to-background activity concentration ratios. Sources 6 mm in diameter or larger can be confidently detected based on the Rose criterion and should have an accurate contrast assignment for the measurement of treatment response. Phantom reconstructions for the NEMA small animal phantom result in a recovery coefficient of 0.21 for

93

the 1 mm rod up to 0.89 for the 5 mm rod. Improvements to the recovery coefficients are noted for this system compared to both PEM and WB PET.

Given the peculiarities of testing an intermediate FOV that is composed of a modular detector system, it is suggested that a hybrid evaluation implementing tests specific to device geometry should be considered when investigating the image quality of an organ-targeted PET camera. Importantly, it is valuable to have results for recovery coefficients from both suggested methods for comparison between the two analyses and for a more clinically analogous description of lesion detectability based on the images of hot spheres in an active background. Given that improved detectability of small sources from increasing spatial resolution is becoming less frequent and impactful, partial volume correction methods may lead to more significant improvements in the future for this type of device.

4 Section 4 – Summary of Thesis and Concluding Remarks

4.1 Conclusion

This research has focused on the development of an advanced solid-state technology for an organ-targeted PET camera and the experimental evaluation of the performance of its first clinical prototype, called the Radialis PET camera. The advantages of the Radialis PET camera are that with an optimized detector architecture it significantly improves the system sensitivity and spatial resolution in comparison to standard WB PET devices. The utilization of this camera for breast-targeted applications is of particular interest because it can circumvent the current shortcomings of X-ray breast screening for imaging dense breasts.

It is observed that this PET camera has a high peak per-slice absolute sensitivity of 3.5% and a high in-plane spatial resolution of (2.3 ± 0.1) mm. Such a high sensitivity with this modular detector design compared to other breast-specific cameras implies that scans with this camera can be performed with reduced levels of radioactivity, and thus will reduce the radiation burden on patient populations. The ability for the scanner to perform for reduced activity loads will not be limited by the dead-time of the system based on the count rate curves that were obtained. Images from the ongoing clinical trials validates the effective utilization of this PET camera for visualization of malignant breast tumors under standard and reduced activities. In fact, high resolution clinical images were obtained at 37 MBq of the injected radiopharmaceutical which represents a 10-fold reduction to the standard dose. This implies the exposure that a patient will receive will not exceed ~1.3 mSv, which is estimated to be equivalent to the effective dose from combined FFDM with DBT. An exposure of that magnitude could prove to be appropriate for

95

screening women with dense breasts as the radiation-induced cancer risk would be similar to current screening methods.

The imaging characteristics of this system were obtained through standardized and custom methods with different phantoms and radiation sources including point sources, linear sources, flood field sources, and phantoms that mimic body parts. The measured in-plane spatial resolution of the scanner was (2.3 ± 0.04) mm for a capillary phantom (consistent with point source resolutions). Spatial linearity of the PET camera is measured to be accurate within 0.1 mm across the entire FOV. Uniformity from both the flood field source and the NEMA image quality phantom were 11.7% and 8.31% respectively. Recovery coefficients from the micro-sphere sources in a hot background range from 0.35 to 0.70 for a 4:1 activity concentration ratio. Recovery coefficients from the NEMA image quality phantom range from 0.21 for the 1 mm and 0.89 for the 5 mm hot rods, respectively. These results show improvements compared to PEM and Whole-Body PET. Based on the contrast to noise ratio within recovery coefficient experiments it was determined that 6 mm sources are detectable under any LBR and, depending on uptake, lesions as small as 4 mm are detectable based on the Rose criterion.

The performance of this prototype device shows overall improvements to other breast-specific PET systems and whole-body PET. The modular detector design which is used allows for a freedom in the design of the detector heads, not limited to the configuration demonstrated here, and may pave the way for other PET cameras that are specifically designed for imaging targeted organs. For the breast design a patient is in sitting position with the planar detector heads positioned on either side of the breast. For cardiac imaging the detectors can be turned vertically and positioned on both sides of the chest, also in a seated position. Prostate imaging conversely

96

has detector heads located above and below the pelvis of the patient lying down on a patient bed. The comparatively small size of detector modules allows integration within other imaging systems such as MRI with minimal adaptation in a PET/MRI system: for brain imaging, the detector blocks can be arranged in an annular configuration (rather than in the 2D planar configuration, which is currently used for breast) and can be integrated with the MRI head coil. The combination of the above advantages makes the proposed PET technology ideal for an integrated PET/MRI system. This would be further improved with new radiotracers that are being developed to allow for more specific characterization of biological function.

5 References

1.   Narayanan, D. & Berg, W. A. Use of Breast-Specific PET Scanners and Comparison with MR Imaging. *Magn. Reson. Imaging Clin. N. Am.* **26**, 265–272 (2018).

2.   Jadvar, H. *et al.* Appropriate use criteria for 18F-FDG PET/CT in restaging and treatment response assessment of malignant disease. *J. Nucl. Med.* **58**, 2026–2037 (2017).

3.   Phelps, M. E. *Physics, instrumentation, and scanners*.

4.   ANGER, H. O. Scintillation Camera With Multichannel Collimators. Ucrl-11387. *UCRL [reports]. U.S. At. Energy Comm.* **31**, 70–86 (1964).

5.   Britvitch, I., Johnson, I., Renker, D., Stoykov, A. & Lorenz, E. Characterisation of Geiger-mode avalanche photodiodes for medical imaging applications. *Nucl. Instruments Methods Phys. Res. Sect. A Accel. Spectrometers, Detect. Assoc. Equip.* **571**, 308–311 (2007).

6.   Yamamoto, S. *et al.* Interference between PET and MRI sub-systems in a silicon-photomultiplier- based PET/MRI system. *Phys. Med. Biol.* **56**, 4147–4159 (2011).

7.   McElroy, D. P., Saveliev, V., Reznik, A. & Rowlands, J. A. Evaluation of silicon photomultipliers: A promising new detector for MR compatible PET. *Nucl. Instruments Methods Phys. Res. Sect. A Accel. Spectrometers, Detect. Assoc. Equip.* **571**, 106–109 (2007).

8.   Wagatsuma, K. *et al.* Comparison between new-generation SiPM-based and conventional PMT-based TOF-PET/CT. *Phys. Medica* **42**, 203–210 (2017).

9.   Reddin, J. S. *et al.* Performance Evaluation of the SiPM-based Siemens Biograph Vision PET/CT System. *2018 IEEE Nucl. Sci. Symp. Med. Imaging Conf. NSS/MIC 2018 - Proc.* 1–5 (2018).

10.   Cherry, S. R. *et al.* Total-body PET: Maximizing sensitivity to create new opportunities for clinical research and patient care. *J. Nucl. Med.* **59**, 3–12 (2018).

11.   Grant, A. M. *et al.* NEMA NU 2-2012 performance studies for the SiPM-based ToF-PET component of the GE SIGNA PET/MR system. *Med. Phys.* **43**, 2334–2343 (2016).

12.   Moliner, L. *et al.* NEMA Performance Evaluation of CareMiBrain dedicated brain PET and Comparison with the whole-body and dedicated brain PET systems. *Sci. Rep.* **9**, 1–10 (2019).

13.   Teixeira, S. C. *et al.* Evaluation of a hanging-breast PET system for primary tumor visualization in patients with stage I-III breast cancer: Comparison with standard PET/CT. *Am. J. Roentgenol.* **206**, 1307–1314 (2016).

14.   García Hernández, T. *et al.* Performance evaluation of a high resolution dedicated breast PET scanner. *Med. Phys.* **43**, 2261–2272 (2016).

15.   Luo, W., Anashkin, E. & Matthews, C. G. Performance evaluation of a PEM scanner using the NEMA NU 4-2008 small animal PET standards. *IEEE Trans. Nucl. Sci.* **57**, 94–103 (2010).

16.   Fowler, A. M. A molecular approach to breast imaging. *J. Nucl. Med.* **55**, 177–180 (2014).

17.   Kalles, V., Zografos, G. C., Provatopoulou, X., Koulocheri, D. & Gounaris, A. The current

status of positron emission mammography in breast cancer diagnosis. *Breast Cancer* **20**, 123–130 (2013).

18. Schilling, K. *et al.* Positron emission mammography in breast cancer presurgical planning: Comparisons with magnetic resonance imaging. *Eur. J. Nucl. Med. Mol. Imaging* **38**, 23–36 (2011).

19. Miladinova, D. Molecular Imaging in Breast Cancer. *Nucl. Med. Mol. Imaging (2010).* **53**, 313–319 (2019).

20. Daube-Witherspoon, M. E. & Muehllehner, G. Treatment of axial data in three-dimensional PET. *J. Nucl. Med.* **28**, 1717–1724 (1987).

21. Herold, C. J. *et al.* Imaging in the age of precision medicine: Summary of the proceedings of the 10th biannual symposium of the international society for strategic studies in radiology. *Radiology* **279**, 226–238 (2016).

22. Griffeth, L. K. Use of Pet/Ct Scanning in Cancer Patients: Technical and Practical Considerations. *Baylor Univ. Med. Cent. Proc.* **18**, 321–330 (2005).

23. Weber, W. A. *et al.* The Future of Nuclear Medicine, Molecular Imaging, and Theranostics. *J. Nucl. Med.* **61**, 263S-272S (2020).

24. Gonzalez, A. J., Sanchez, F. & Benlloch, J. M. Organ-Dedicated Molecular Imaging Systems. *IEEE Trans. Radiat. Plasma Med. Sci.* **2**, 388–403 (2018).

25. Hendrick, R. E. Radiation doses and cancer risks from breast imaging studies. *Radiology* **257**, 246–253 (2010).

100

26. Catana, C. The Dawn of a New Era in Low-Dose PET Imaging. *Radiology* **290**, 657–658 (2019).

27. O'Connor, M. K. *et al.* Comparison of radiation exposure and associated radiation-induced cancer risks from mammography and molecular imaging of the breast. *Med. Phys.* **37**, 6187–6198 (2010).

28. Reznik, Alla; Bubon, Oleksandr; Teymurazyan, A. Tileable block detectors for seamless block detector arrays in Positron Emission Mammography. vol. 4 (2017).

29. Poladyan, H., Bubon, O., Teymurazyan, A., Senchurov, S. & Reznik, A. Gaussian position-weighted center of gravity algorithm for multiplexed readout. *Phys. Med. Biol.* **65**, (2020).

30. Poladyan, H., Bubon, O., Teymurazyan, A., Senchurov, S. & Reznik, A. Gain invariant coordinate reconstruction for SiPM-Based pixelated gamma detectors with multiplexed readout. *IEEE Trans. Instrum. Meas.* **69**, 4281–4291 (2020).

31. Shepp, L. A. & Vardi, Y. Maximum Likelihood Reconstruction for Emission Tomography. *IEEE Trans. Med. Imaging* **1**, 113–122 (1982).

32. Alenius, S. & Ruotsalainen, U. Bayesian image reconstruction for emission tomography based on median root prior. *Eur. J. Nucl. Med.* **24**, 258–265 (1997).

33. *NEMA NU 4-2008. Performance measurements of Small Animal Positron Emission Tomographs.* (National Electrical Manufactureres Association, 2008).

34. Hallen, P., Schug, D. & Schulz, V. Comments on the NEMA NU 4-2008 Standard on Performance Measurement of Small Animal Positron Emission Tomographs. *EJNMMI*

Phys. **7**, (2020).

35. Schneider, C. A., Rasband, W. S. & Eliceiri, K. W. NIH Image to ImageJ: 25 years of image analysis. *Nat. Methods* **9**, 671–675 (2012).

36. Weissler, B. *et al.* MR compatibility aspects of a silicon photomultiplier-based PET/RF insert with integrated digitisation. *Phys. Med. Biol.* **59**, 5119–5139 (2014).

37. MacDonald, L. *et al.* Clinical Imaging Characteristics of the Positron Emission Mammography Camera: PEM Flex Solo II. *J. Nucl. Med.* **50**, 1666–1675 (2009).

38. Smith, M. F., Majewski, S. & Raylman, R. R. Positron Emission Mammography with Multiple Angle Acquisition. *IEEE Nucl. Sci. Symp. Med. Imaging Conf.* **3**, 1892–1896 (2002).

39. Evaluating Positron Emission Mammography Imaging of Suspicious Breast Abnormalities" (ClinicalTrials.govIdentifier: NCT03520218).

40. Gong, K., Cherry, S. R. & Qi, J. On the assessment of spatial resolution of PET systems with iterative image reconstruction. *Phys. Med. Biol.* **61**, N193–N202 (2016).

41. Muzahir, S. Molecular Breast Cancer Imaging in the Era of Precision Medicine. *Am. J. Roentgenol.* **215**, 1512–1519 (2020).

42. Schilling, K. *et al.* Positron emission mammography in breast cancer presurgical planning: Comparisons with magnetic resonance imaging. *Eur. J. Nucl. Med. Mol. Imaging* **38**, 23–36 (2011).

43. Brem, R. F. *et al.* Breast-specific gamma imaging with 99mTc-Sestamibi and magnetic
102

resonance imaging in the diagnosis of breast cancer - A comparative study. *Breast J.* **13**, 465–469 (2007).

44. Pisano, E. D. *et al.* Diagnostic performance of digital versus film mammography for breast-cancer screening. *N Engl J Med* **353**, 1773–1783 (2005).

45. National Cancer Institute Breast Cancer Surveillance Consortium website. Distribution of key variables: BI-RADS breast density. (2014).

46. Caldarella, C., Treglia, G. & Giordano, A. Diagnostic performance of dedicated positron emission mammography using fluorine-18-fluorodeoxyglucose in women with suspicious breast lesions: A meta-analysis. *Clin. Breast Cancer* **14**, 241–248 (2014).

47. Reynés-Llompart, G. *et al.* Performance characteristics of the whole-body discovery IQ PET/CT system. *J. Nucl. Med.* **58**, 1155–1161 (2017).

48. Delso, G. *et al.* Performance Measurements of the Siemens mMR Integrated Whole-Body PET/MR Scanner. *J. Nucl. Med.* **52**, 1914–1922 (2011).

49. Hruska, C. B. & O'Connor, M. K. Nuclear imaging of the breast: Translating achievements in instrumentation into clinical use. *Med. Phys.* **40**, 1–23 (2013).

50. Schilling K, Narayanan D, K. J. Effect of Breast Density, Menopausal Status, and Hormone Use in High Resolution Positron Emission Mammography. in *Radiological Society of North America* (2008).

51. Shilling, K. New Breast Imaging Modalities Reveal Cancers as Small as a Single Millimeter. *RSNA, 94th Sci. Assem. Annu. Meet. Radiol. Soc. North Am.* (2008).

52.   Chong, T. "Frost & Sullivan Names Naviscan a Leader in the Future of Molecular Breast Imaging". *Frost & Sullivan* (2008).

53.   Moliner, L. *et al.* Design and evaluation of the MAMMI dedicated breast PET. *Med. Phys.* **39**, 5393–5404 (2012).

54.   Soriano, A. *et al.* Performance evaluation of the dual ring MAMMI breast PET. *IEEE Nucl. Sci. Symp. Conf. Rec.* 13–16 (2013) doi:10.1109/NSSMIC.2013.6829103.

55.   Vandenberghe, S., Moskal, P. & Karp, J. S. State of the art in total body PET. *EJNMMI Phys.* **7**, (2020).

56.   Pan, T. *et al.* Performance evaluation of the 5-Ring GE Discovery MI PET/CT system using the national electrical manufacturers association NU 2-2012 Standard. *Med. Phys.* **46**, 3025–3033 (2019).

57.   Miller, M. A., Molecular, A. & Physics, I. Vereos White Paper: Focusing on high performance. *K. Philips N.V.* 16 (2016).

58.   Van Sluis, J. *et al.* Performance characteristics of the digital biograph vision PET/CT system. *J. Nucl. Med.* **60**, 1031–1036 (2019).

59.   MacDonald, L. R. *et al.* Positron emission mammography image interpretation for reduced image count levels. *J. Nucl. Med.* **57**, 348–354 (2016).

60.   Narayanan, D. & Berg, W. A. Use of breast-specific PET scanners and comparison to MRI. *Magn. Reson. Imaging Clin. N. Am.* **26**, 265–272 (2018).

61.   Hathi, D. K. *et al.* Evaluation of primary breast cancers using dedicated breast PET and

whole-body PET. *Sci. Rep.* **10**, 21930 (2020).

62. Cherry SR, Phelps ME. Positron emission tomography: methods and instrumentation. In: Sandler MP, Coleman RE, Wackers FJT, Patton JA, Gottschalk A, Hoffer PB, eds. Diagnostic Nuclear Medicine. 3rd ed. Baltimore, MD: Williams & Wilkins; 1996:139 – 159 (1996).

63. Hoffman EJ, Phelps ME. Positron emission tomography: principles and quantification. In: Phelps ME, Mazziotta JC, Schelbert RH, eds. Positron Emission Tomography and Autoradiography: Principles and Applications for the Brain and Heart. New York, NY: Raven (1986).

64. Shkumat, N. A. *et al.* Investigating the limit of detectability of a positron emission mammography device: A phantom study. *Med. Phys.* **38**, 5176–5185 (2011).

65. Stiles, J. *et al.* Evaluation of a High-Sensitivity Organ-Targeted PET Camera. *'Submitted to' Med. Phys.* 5 (2021).

66. Øen, S. K., Aasheim, L. B., Eikenes, L. & Karlberg, A. M. Image quality and detectability in Siemens Biograph PET/MRI and PET/CT systems—a phantom study. *EJNMMI Phys.* **6**, 1–16 (2019).

67. *NEMA NU 2-2018. Performance Measurements of Positron Emission Tomographs.* (National Electrical Manufactureres Association, 2018).

68. Nema. NEMA Standards Publication NU 1-2007. 1–39 (2007).

69. Nuclear Medicine Committee. Computer-Aided Scintillation Camera Acceptance Testing.

105

1–44 (1982).

70.   Snyder, D. L., Miller, M. I., Thomas, L. J. & Politte, D. G. Noise and Edge Artifacts in Maximum-Likelihood Reconstructions for Emission Tomography. *IEEE Trans. Med. Imaging* **6**, 228–238 (1987).

71.   Goertzen, A. L. *et al.* NEMA NU 4-2008 comparison of preclinical PET imaging systems. *J. Nucl. Med.* **53**, 1300–1309 (2012).

72.   Bao, Q., Newport, D., Chen, M., Stout, D. B. & Chatziioannou, A. F. Performance Evaluation of the Inveon Dedicated PET Preclinical Tomograph Based on the NEMA NU-4 Standards. *J. Nucl. Med.* **50**, 401–408 (2009).

73.   Gu, Z. *et al.* Performance evaluation of HiPET, a high sensitivity and high resolution preclinical PET tomograph. *Phys. Med. Biol.* **65**, (2020).

74.   Son, J. W. *et al.* SimPET: a Preclinical PET Insert for Simultaneous PET/MR Imaging. *Mol. Imaging Biol.* **22**, 1208–1217 (2020).

75.   Alavi, A., Werner, T. J., Høilund-Carlsen, P. F. & Zaidi, H. Correction for Partial Volume Effect Is a Must, Not a Luxury, to Fully Exploit the Potential of Quantitative PET Imaging in Clinical Oncology. *Mol. Imaging Biol.* **20**, 5–7 (2018).

76.   Cysouw, M. C. F. *et al.* Impact of partial-volume correction in oncological PET studies: a systematic review and meta-analysis. *Eur. J. Nucl. Med. Mol. Imaging* **44**, 2105–2116 (2017).

77.   Hoetjes, N. J. *et al.* Partial volume correction strategies for quantitative FDG PET in

oncology. *Eur. J. Nucl. Med. Mol. Imaging* **37**, 1679–1687 (2010).

78.   Soret, M., Bacharach, S. L. & Buvat, I. Partial-volume effect in PET tumor imaging. *J. Nucl. Med.* **48**, 932–945 (2007).